Journal of Chemical Health Risks
www.jchr.org
JCHR (2025) 15 (03), 1161-1190 | ISSN: 2251-6719

Biogenic Extract-Mediated Synthesis of Mg-Ni Co-Doped TiO_2 Nanomaterial: A Sustainable visible light sensitized Catalyst for Dye and Bacterial Decontamination

Raffiunnisa[1,2], Siva RaoTirukkovalluri[2*], Divya Gorli[2], S. Sai Supriya[2], Sandhya Rani Nayak[2], Genji Jai Sree[2], Nageswararao Kadiyala[2]

[1]Department of Chemistry, Aditya university, Surampalem, Andhra Pradesh, 533437, India.
[2]Department of Chemistry, Andhra University, Visakhapatnam, Andhra Pradesh, 530013, India.
Corresponding Author: Siva RaoTirukkovalluri, Professor, Department of Chemistry, Andhra University, Visakhapatnam, Andhra Pradesh, 530013, India.

(Received: 15 March 2025 Revised: 20 April 2025 Accepted: 26 May 2025)

KEYWORDS
MNT-2L2 Photocatalyst, Sol-gel method, Photocatalysis, Degradation of dye, Acid red 249 dye, antibacterial activity.

ABSTRACT:
Tuning the optical and structural properties of TiO_2 nanoparticles through Mg and Ni co-doping, utilizing lemon juice as a capping agent via the sol-gel method for effective dye and microbial decontamination under visible light irradiation. The synthesized Nano catalysts were characterized using PXRD, which confirmed the formation of the anatase phase. The narrowing of the band gap was determined by UV-Vis DRS, revealing a reduction from 3.2 eV for undoped TiO_2 to 2.7 eV for MNT-2 and 2.5 eV for MNT-2L2. TEM and SEM techniques were employed to determine the lower particle sizes of MNT-2L2 6.2 nm compare to UDT and MNT2, which exhibited a spherical shape with smooth morphology. BET surface area analysis indicated a significant increase in surface area 61.89 m^2/g for UDT, 102.34 for MNT2 and 182.79 m^2/g for MNT-2L2.The substitutional doping of Mg and Ni into the TiO_2 lattice was analysed using FTIR and XPS techniques. Additionally, photoluminescence analysis was conducted to evaluate reduced electron-hole recombination and the formation of hydroxyl radicals. The EIS plot was used to examine charge transport and the flat band potential, which lies below the conduction band and hinders electron-hole recombination. Electrochemical analysis was performed to investigate the redox potential, peak current, diffusion coefficient in dark and visible light.VB-XPS measurements were performed to determine the valence band position after doping. Finally, the catalytic efficiency of the MNT-2L2 Nano catalyst was assessed by the degradation of Acid Red 249 dye, achieving complete degradation within 80 minutes. The catalyst was also evaluated for its antibacterial activity, demonstrating a zone of inhibition against Vibrio cholerae comparable to that of standard chloramphenicol.

Journal of Chemical Health Risks
www.jchr.org
JCHR (2025) 15 (03), 1161-1190 | ISSN: 2251-6719

1. Introduction

Nanomaterials, characterized by at least one dimension within the 1–100 nm range, possess a high surface area, quantum effects, and enhanced mechanical, electrical, and optical properties. They are classified based on their dimensionality and are extensively used in fields such as electronics, medicine, energy storage, and catalysis [1]. As semiconductors, these materials exhibit tunable bandgaps, quantum confinement effects, and high charge mobility, making them crucial for applications in photo detectors, solar cells, medical imaging, and pollution control [2]. Semiconductor nanomaterials play a crucial role in pollution removal through advanced oxidation processes (AOPs), such as photocatalysis. Among these, titanium dioxide (TiO_2) is one of the most effective choices. It is an n-type semiconductor with a bandgap of approximately 3.3 eV, is non-toxic, and exhibits excellent properties, including low resistivity, high thermal and chemical stability, and outstanding photocatalytic activity [3].

However, the practical applications of this material are often limited by its wide bandgap (3.2 eV) and the recombination of electron-hole pairs, which reduces its photocatalytic efficiency under visible light [4]. To overcome these inherent limitations, especially in photocatalysis, various strategies have been explored. Sood et al. conducted a study showing that Fe (III)-doped TiO_2 nanoparticles have a small size, leading to a larger surface area and increased visible light absorption. This effectively suppresses charge carrier recombination, thereby enhancing photocatalytic activity [5]. Similarly, Zhang et al. found that Cu doping introduces additional energy levels within the TiO_2 bandgap, serving as traps for charge carriers. This mechanism reduces electron-hole recombination and improves photocatalytic efficiency under visible light exposure [6]. Furthermore, Soundarya et al. successfully synthesized Pt-doped TiO_2 nanotubes (NTbs) using the hydrothermal method. Their study demonstrated enhanced hydrogen (H_2) generation through photocatalytic water splitting by effectively minimizing electron-hole recombination. This improvement is also attributed to the material's high electrical conductivity and stable electrical properties, with a low impedance of 79 Ohms [7].

Li et al. discovered that 4% W-doped TiO_2 exhibited the highest photocatalytic activity, which was 3.5 times greater than that of undoped TiO_2. Doping introduced new energy levels within the bandgap, acting as electron trapping centers that prolonged the lifetime of charge carriers [8]. Similarly, Yu et al. investigated the synthesis of N-doped TiO_2 nanoparticle photocatalysts using the sol-gel method, with NH_4Cl as the nitrogen source, followed by calcination at a specific temperature. The incorporation of nitrogen into the TiO_2 lattice led to a narrowed bandgap, significantly enhancing photocatalytic activity [9]. Ghumro et al. successfully synthesized carbon-doped TiO_2 nanoflakes (C-TNFs) using a simple hydrothermal method with different carbon sources. The incorporation of carbon into the TiO_2 lattice, either by replacing a titanium or oxygen atom to form Ti–C or C–O–Ti bonds, led to the creation of a hybrid orbital just above the valence band of TiO_2. This structural modification significantly enhanced photocatalytic activity under visible light[10]. Similarly, Thakur et al. reported that doping TiO_2 with Ni^{2+} and Cu^{2+} ions altered the electronic band structure, effectively narrowing the

Journal of Chemical Health Risks
www.jchr.org
JCHR (2025) 15 (03), 1161-1190 | ISSN: 2251-6719

bandgap. This allowed the nanoparticles to absorb a broader range of light while also suppressing electron-hole recombination, resulting in improved photocatalytic efficiency [11]. Furthermore, Talat-Mehrabad et al. found that the bandgap of Mg and Ag co-doped TiO_2-P25 was smaller than that of undoped TiO_2. The narrowing of the bandgap caused a shift in the absorption band toward the visible light region, reducing electron-hole recombination and increasing the catalytic activity [12]. Erbium (Er) and Magnesium (Mg) co-doped titanium dioxide (TiO_2) catalysts were synthesized using a straightforward hydrothermal method and investigated for their photovoltaic performance in perovskite solar cells. Among alkaline earth metals, Mg^{2+} stands out as a promising dopant due to its ionic radius (0.72 Å), which closely matches that of Ti^{4+} [13]. Magnesium plays a crucial role in titanium dioxide by aiding in band gap reduction. This is achieved through the formation of an additional energy level just above the valence band, arising from the interaction between the 2p orbitals of magnesium and oxygen ions [11]. Sun et al. successfully synthesized Fe–Ni co-doped TiO_2 nanoparticles via an alcohol-thermal process using tetra-butyl titanate as a precursor. The incorporation of Fe and Ni inhibits crystal growth and enhances visible light absorption, leading to a red shift due to band gap narrowing while also suppressing electron-hole recombination [14]. A comprehensive review of existing literature suggests that the combination of Mg and Ni with other metal ion dopants exhibits outstanding properties, effectively reducing the band gap and extending charge carrier recombination time.

This study focuses on the synthesis of Mg and Ni co-doped TiO_2 using a biogenic extract (lemon juice) through a sol-gel approach, highlighting its potential for enhanced photocatalytic and photovoltaic applications. Kim et al. successfully synthesized titanium dioxide (TiO_2) doped with 8 wt.% nickel using the mechanical alloying method. Photoluminescence analysis revealed that the newly observed absorption is likely attributed to the localization of the trapping level near either the valence or conduction band [15]. Additionally, Ni^{2+} has an ionic radius of 0.72 Å, which is very close to the 0.68 Å radius of Ti^{4+}. This similarity facilitates the substitution of Ti^{4+} with Ni^{2+}, effectively reducing electron-hole recombination and enhancing surface photocatalysis [16]. Athira et al. investigated the synthesis of Mg-doped TiO_2 nanoparticles (0.3 M and 0.4 M) using the sol–gel method. Their findings showed that incorporating Mg into the TiO_2 lattice resulted in a more significant red shift and broader absorption spectrum. The band gap values were reduced from 3.02 eV to 2.87 eV [17]

Lemon juice is a rich source of citric acid, which functions as an efficient capping agent by inhibiting surface chemical reactivity. The citrate ions form strong coordination bonds with Ti^{4+} ions, significantly stabilizing the molecules and preventing nanoparticle aggregation. In addition to controlling the shape, size, and agglomeration behaviour of TiO_2 nanoparticles, citric acid has also been instrumental in achieving phase selectivity [18]. Lemon juice acts as a capping agent due to the presence of organic acids (such as citric acid) and biomolecules that bind to the surface of nanoparticles, preventing agglomeration and controlling their growth. These compounds help stabilize the nanoparticles, leading to uniform size distribution and enhanced surface properties. Citrus lemon extract served as a natural source of citric acid, which played a

Journal of Chemical Health Risks
www.jchr.org
JCHR (2025) 15 (03), 1161-1190 | ISSN: 2251-6719

dual role in the synthesis of TiO_2 nanoparticles. It functioned as a reducing agent, facilitating the hydrolysis of titanium butoxide precursor molecules, and as a capping agent, minimizing the surface reactivity of the nanoparticles [19].

Further, to evaluate the photocatalytic performance of the synthesized catalyst (MNT-2L2), degradation experiments were conducted using Acid Red 249 dye as a model pollutant. Acid Red 249 belongs to the class of synthetic azo dyes widely utilized in various industries, including textiles, leather, food, cosmetics, and paper. These dyes are water-soluble and commonly used for colouring protein fibres such as wool, silk, and nylon, where they form ionic bonds with the fibres to produce a vibrant red colour. Additionally, Acid Red 249 is frequently employed in biological staining and laboratory research due to its ability to bind to acidic or basic components within cells. Given its extensive industrial applications, Acid Red 249 has a high potential to contaminate aquatic environments. Vibrio cholerae is a Gram-negative, comma-shaped bacterium known for its high motility, which is facilitated by a single polar flagellum. Belonging to the Vibrionaceae family, this microorganism is the causative agent of cholera, a severe diarrheal disease. Cholera is an acute illness primarily characterized by profuse watery diarrhea, vomiting, and extreme dehydration, which can be life-threatening if left untreated [21,22]. The infection is primarily transmitted through the ingestion of contaminated food or water. Due to its significant impact on public health, Vibrio cholerae has been selected as the model pathogen for this study.

2. Experimental

2.1 Materials:

Titanium, Magnesium, Nickel are Titanium tetra n-butoxide ($Ti(OBu)_4$) from E-Merck Germany, $Mg(NO_3)_2.6H_2O$ from Hi-media-India, and $Ni(NO_3)_2.6H_2O$ from Hi-media, India were used as a precursors for the synthesis of Mg-Ni cooped TiO_2 nanomaterial. The solvents used in this process is nitric acid (HNO_3) from E-Merck Germany and high-quality ethanol from Hayman-UK. All solutions were made using milli-Q water, and the chemicals were used without any purification. Natural lemon juice was used as a capping agent. Acid red 249 obtained from Hi-media, India ($C_{29}H_{20}C_lN_3Na_2O_{10}S_3$), a model dye used as a pollutant for the efficacy of the synthesized catalyst.

2.2 Preparation of Magnesium and Nickel Co-doped TiO_2 Nanomaterials using sol gel method via lemon juice:

Magnesium and nickel co-doped TiO_2 can be produced using sol-gel method. 20 mL of Titanium precursor and the 40 mL of ethanol are acidified with 3.2 mL of HNO_3 in a 150 mL Pyrex glass vessel (beaker-1) and stirred for 30 minutes. 40 mL of ethanol and 7.2 mL of water were taken in Beaker-2 to dissolve the necessary weight percentages of magnesium and nickel dopants (the weight percentages and name assigned to each combination was given in table-1). The mixture was stirred for 30 minutes. Subsequently solution in beaker-2 was added in beaker-1 drop wisely while stirring the solution in beaker-1. Continuing the stirring until the sol formation and then the sol was allowed to ageing in dark for the formation of gel for 48 hours. Once the gel had dried for 24 hours at 72^0C and ground into a fine powder until fine powder. A muffle furnace was used to calcine the fine powder for 5 hours at 450^0C and then again

Journal of Chemical Health Risks
www.jchr.org
JCHR (2025) 15 (03), 1161-1190 | ISSN: 2251-6719

grounded for 2 hours and kept in amber-colored, airtight glass bottles.

Experiments were conducted for the degradation of Acid red 249 dye and the results were discussed in section-4, from that a best catalyst (MNT2) was selected. Further to increase the rate of degradation of the dyes using the catalyst, the surface area of the catalyst plays a pivotal role for enhancing the rate of degradation. Hence, the best catalyst was again prepared the identical procedure along with capping agent by adding lemon juice. In this process, three samples were prepared by taking 5 ml,10 ml and 15 ml of diluted lemon juice added after sol formation and Continuing the stirring for 10 minutes and allowed in dark for aging until gel formation and the remain same procedure was continued as mention above. By using same procedure, prepared undoped TiO_2 without adding of dopants and capping agent.

Table-1. Different weight percentages dopants

Catalyst code	**Mg weight %**	**Ni weight%**
UDT (Undoped TiO_2)	NIL	NIL
MNT-1(Magnesium and Nickel doped TiO_2-1)	0.25	0.75
MNT-2(Magnesium and Nickel doped TiO_2-2)	0.5	0.5
MNT-3(Magnesium and Nickel doped TiO_2-3)	0.75	0.25
MNT-4(Magnesium and Nickel doped TiO_2-4)	1.0	0.25
MNT-5(Magnesium and Nickel doped TiO_2-5)	1.0	0.5

Table-2. Different weight percentages of dopants and Tailoring agent

Catalyst code	**Magnesium weight %**	**Nickel weight %**	**Lemon juice (Scissoring agent)**
MNT-2L1(L-Lemon juice)	0.5	0.5	5 mL
MNT-2L2(L-Lemon juice)	0.5	0.5	10 mL
MNT-2L3(L-Lemon juice)	0.5	0.5	15 mL

2.3 An illustration of the various instrumental methods used for as synthesized catalyst characterization:

The band gaps and absorption edges of the catalysts were measured using a Shimadzu 3600 UV-Vis DRS spectrophotometer. Pristine TiO_2 and co-doped samples were mixed with $BaSO_4$ to assess reflectance within the 200–800 nm range and determine the band gap. $BaSO_4$ was used as a reference during the measurement process. The instrumental method of Powder X-ray Diffraction (PXRD) was employed to determine the crystalline phase of both pristine and co-doped Mg/Ni TiO_2 using a model Ultima IV-Rigaku diffractometer with a Cu Kα anode (λ = 1.5406 nm). The average crystallite size of the samples was calculated using the Debye-Scherrer equation based on the FWHM results. The PHI Quantum ESCA Microprobe XPS system was used to determine the oxidation states and elemental composition of the catalyst. The spectra were recorded using X-ray radiation at 1253.6 eV with an Al Kα source

Journal of Chemical Health Risks
www.jchr.org
JCHR (2025) 15 (03), 1161-1190 | ISSN: 2251-6719

operating at 250 W, 16 mA current, and 12.5 kV voltage. The selected area electron diffraction (SAED) pattern, along with the size and shape of the catalysts, was analyzed using a LaB_6 electron gun connected to a 200-kV source. High-resolution transmission electron microscopy (HRTEM) provided a point resolution of 0.23 nm and a lattice resolution of 0.14 nm. The HRTEM model used for the analysis was Jeol/EM 2100. The surface morphology was analyzed using a Field Emission Gun Scanning Electron Microscope (FEG-SEM) of model JEOL JSM 7600F, alongside an Energy Dispersive X-ray spectrophotometer (EDX) operating at 20 kV to assess the elemental composition. Using an X-ray tube with a maximum voltage of 50kV and a 1mA Rh target (XGT 5200, Horiba, Japan), X-ray fluorescence (XRF) was employed to determine the elemental composition of the catalyst. The Brunauer-Emmett-Teller (BET) surface area analyzer (Model: GeminiVII2390 series micro metrics) was utilized to assess the pore size, surface area, and pore volume of the Mg and Ni doped photocatalyst. The instrument utilized for the analysis FTIR, was the Bruker 3000 Hyperion Microscope paired with the Vertex 80 FTIR System, in Germany. The FTIR spectra of both doped and undoped catalysts were recorded in the range of 4000-400 cm^{-1}. A system of 150V PMT UV-visible spectrophotometers was employed for the analysis of photoluminescence spectra to investigate the extent and rate of dye degradation. This PL is utilized for assessing the degree of formation of hydroxyl radicals and for determining electron-hole recombination. The pH of the reaction mixture was carefully monitored and adjusted throughout the dye degradation process utilizing Elico's digital pH meter (model IIIE, EI).

2.4 Procedure for photo catalytic degradation of Acid red 249 dye and antibacterial activity:

a) The photocatalytic reactions were conducted under visible light to assess the catalytic efficiency of the prepared MNT-2L2 catalysts while optimizing the reaction parameters. The photocatalytic process involved dispersing the required amount of catalyst, adjusting the pH with 0.1 M HCl or 0.1 M NaOH, and stirring the mixture for 5–10 minutes before introducing 100 mL of Acid Red 249 dye. The sample prepared was then exposed to visible light. For the experimental setup, a 400 W metal halide lamp (35,000 lumens, Osram, India) fitted with a UV filter (Oriel No. 51472) served as the visible light source, positioned 20 cm from the reaction mixture. To maintain ambient temperature and minimize infrared radiation interference, cold water was circulated around the reaction beaker.

A reaction beaker with 100 mL of Acid red 249 dye solution and a designated quantity of catalyst at a specified pH was swirled continuously for 30 minutes in darkness to achieve equilibrium between the dye and the photocatalyst surface. After exposing the reaction mixture to visible light for degradation, 5 mL aliquots of the sample were systematically collected at regular time intervals using Millipore syringe. And the absorbance was measured at 540 nanometers (λ_{max}). The formula for calculating degradation percentage is employed to determine the percentage of degradation at each time interval. The degradation percentage of Acid red 249 dye was quantified using the following formula.

Percentage of degradation = $A_0 - A_t/A_0 \times 100$

b) Although TiO_2 is remarkably potent in eliminating microbes, but its efficiency is

Journal of Chemical Health Risks
www.jchr.org
JCHR (2025) 15 (03), 1161-1190 | ISSN: 2251-6719

influenced by particle size and surface area. Nanoparticles with smaller dimensions exhibit enhanced antimicrobial activity due to their increased surface area contains more active sites. In this study, Bactericidal tests were conducted on a synthesized high-surface-area sample, MNT-2L2, using the agar well diffusion method to evaluate its antibacterial properties.

To facilitate bacterial growth, nutrient agar and potato dextrose agar were used as culture media. These media were sterilized in an autoclave at 121°C under 15 psi pressure for 20 minutes. Before pouring the agar, Petri dishes were carefully sanitized and left in a sterile environment to solidify the agar -agar nutrient broth. Once the agar was set, bacterial broth cultures were evenly spread across the plates using an L-shaped glass rod to ensure uniform distribution.

Each Petri dish contained four wells, created using a sterile corkborer with a diameter of 6 mm. Three of these wells were filled with different concentrations of the MNT-2L2 sample (400 µg/mL, 600 µg/mL, and 800 µg/mL), while the fourth well contained a standard antibacterial agent at a concentration of 50 µg/mL. Following the sample placement, the plates were exposed to visible light for 10 minutes.

After light illumination, the bacterial culture plates were incubated at 37°C for 24 hours. The antimicrobial activity of the MNT-2L2 nanoparticles was then evaluated by measuring the inhibition zone. The effectiveness of the sample was determined by comparing the inhibition zone measurements with standard reference values using a millimeter antibiotic scale.

3. Result and Discussion

3.1 Analysis of XRD:

The powder XRD patterns of the doped and undoped TiO_2 samples are presented in Fig. 2. The 2θ peak values of undoped TiO_2 (JCPDS card no. 21-1272) were observed at 25.3°, 37.8°, 48.2°, 54.8°, 55.2°, 62.7°, and 75.2°. The 2θ values of all the samples indicated the presence of the anatase phase at 25.3°[23]. A slight shift in the peaks was observed for MNT-2 and MNT-2L2 compared to undoped TiO_2, suggesting the incorporation of Mg and Ni elements into the host lattice of TiO_2 nanoparticles.

Fig. 2 illustrates that the 2θ peak values of 25.5° (MNT-2L2), 25.6° (MNT-2), and 25.3° (UDT) indicate that the incorporation of Mg and Ni into the TiO_2 lattice caused a minor shift in the anatase peak values of the two catalysts. The average crystallite size was determined using the Debye-Scherrer equation [UDT-(11.9), MNT-1 (8.3), MNT-2 (8.0), MNT-3 (8.3), MNT-4 (8.8), MNT-2L1 (6.7), MNT-2L2 (6.2), MNT-2L3 (6.3)]. MNT-2L2 exhibits a smaller crystallite size of 6.2 nm compared to MNT-2 at 8.0 nm and UDT at 11.9 nm, as detailed in Table 3. This is evident from the higher dislocation density and grain strain. An increased dislocation density enhances grain strain, leading to more distinct grain boundaries due to grain shrinkage and catalyst-induced defects, ultimately reducing the crystallite size UDT-11.9 [24,51].

Table-3. Catalyst-induced defects

Catalyst code	Crystallite size	Band gap	Micro strain	Dislocation density (m^2)	Texture co-efficient (101)
UDT	11.9 nm	3.2eV	0.12	$2.8X10^{14}$	0.92
MNT-2	8.0 nm	2.74eV	0.50	$2.4\ X10^{14}$	0.94

Journal of Chemical Health Risks
www.jchr.org
JCHR (2025) 15 (03), 1161-1190 | ISSN: 2251-6719

MNT-2L2	6.2 nm	2.50eV	0.58	$1.63X10^{14}$	0.98

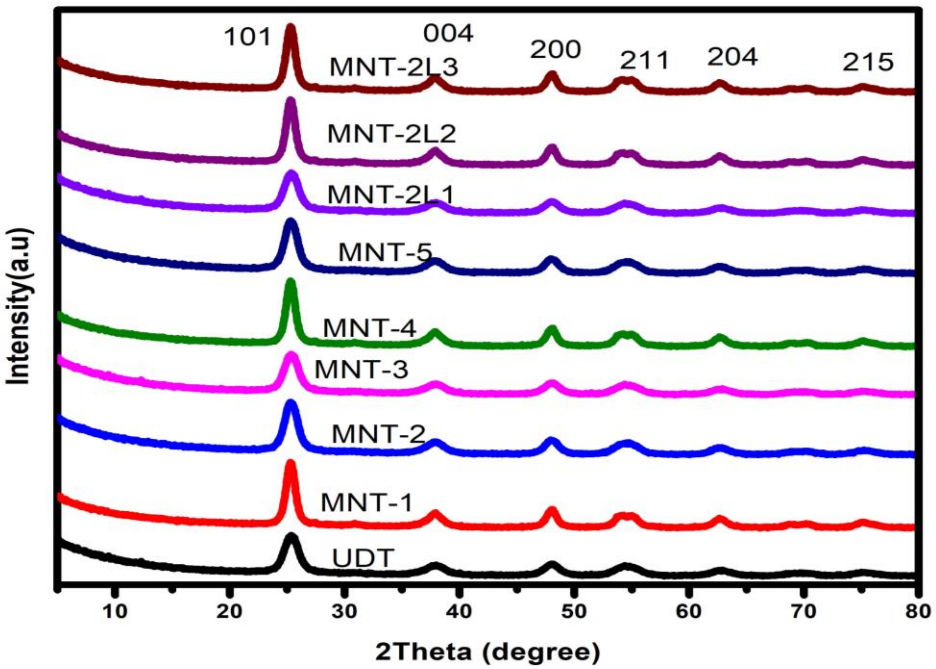

Fig. 2 shows the PXRD of all catalyst

3.2 Analysis of UV-Vis DRS:

The bandgap energy of undoped TiO_2 and MNT catalysts was evaluated using UV-visible diffuse reflectance spectroscopy. Figures 3a and b illustrate the absorbance spectra of all synthesized undoped and co-doped catalysts, highlighting the significant tailing absorbance of MNT-2L2 in the visible light region. Figures 3c and d show that the bandgap energy of MNT-2 shifted to 2.74 eV, whereas other co-doped samples exhibited values ranging from 2.78 to 2.80 eV. In contrast, the pristine TiO_2 sample maintained a bandgap of 3.2 eV. These variations in bandgap energy can be attributed to the substitutional doping of TiO_2 with magnesium (Mg) and nickel (Ni). The bandgap values were determined using the Kubelka-Munk formalism, where the reflectance spectra [F(R)] were analyzed to construct Tauc plots (Fig. 3c). The calculated bandgap energies for pristine TiO_2 (3.2 eV) and the co-doped samples MNT-1 (2.77 eV), MNT-2 (2.74 eV), MNT-3 (2.78 eV), MNT-4 (2.75 eV), and MNT-5 (2.80 eV) ranged between 3.2 and 2.74 eV. Among these, the MNT-2 catalyst exhibited the lowest bandgap of 2.74 eV.

Further modification of MNT-2 using a lemon juice-based tailoring agent resulted in additional bandgap reductions: MNT-2L1 (2.56 eV), MNT-2L2 (2.50 eV), and MNT-2L3 (2.55 eV), with MNT-2L2 reaching the lowest value of 2.50 eV (Fig. 3c). These findings indicate that the incorporation of Mg and Ni, along with the capping agent, enhanced the absorption intensity and extended the photoelectric response of the catalysts shifted towards the visible spectrum [25].

Journal of Chemical Health Risks
www.jchr.org
JCHR (2025) 15 (03), 1161-1190 | ISSN: 2251-6719

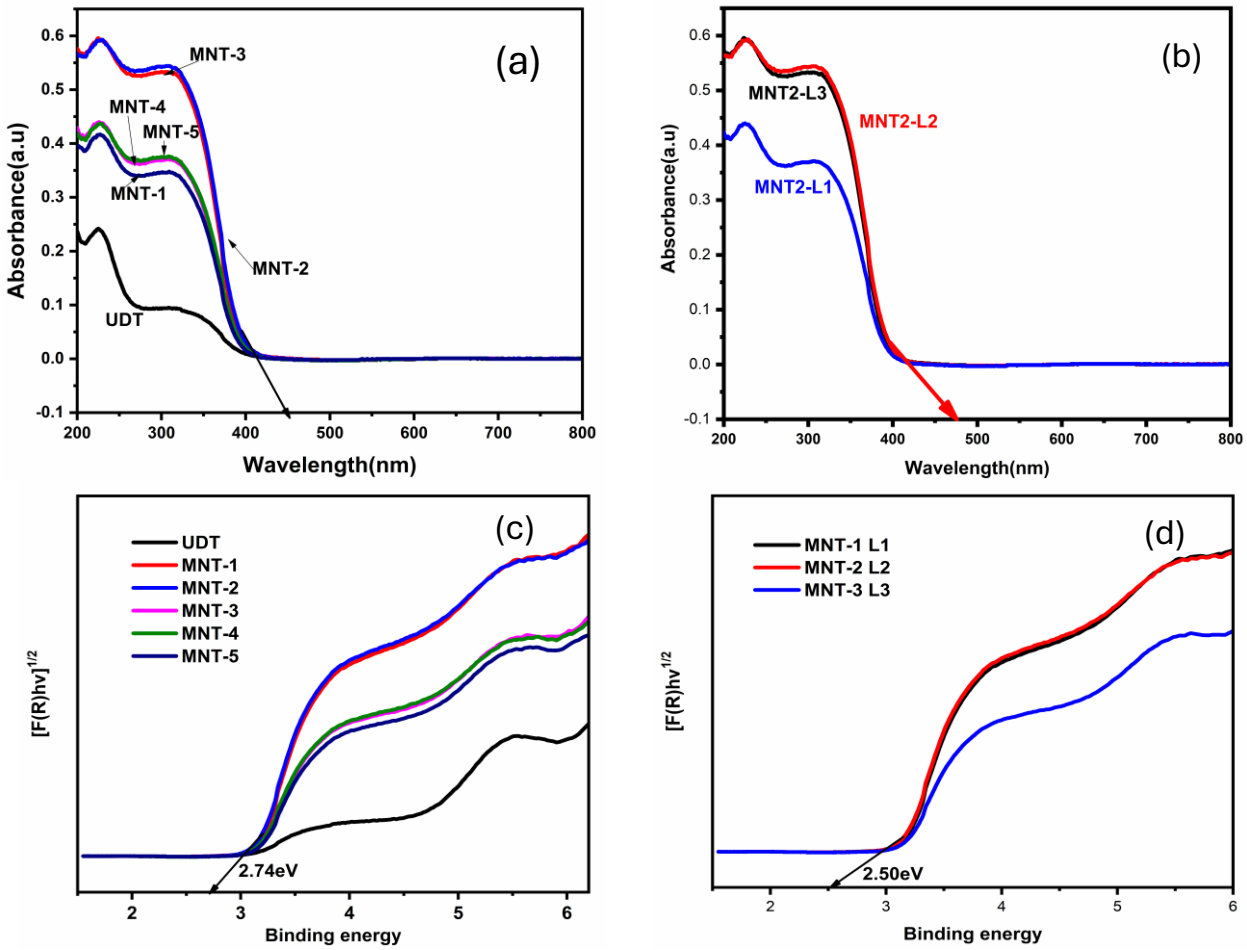

Fig. 3 Shows the UV-Vis DRS of a) &b) Absorbance vs Wavelength of catalysts UDT, MNT-1 to MNT-5 & MNT-2L1 to MNT-2L3 c) &d) $[F(R)hv)^{1/2}]$ vs the photon energy (hν) for UDT, MNT-1 to MNT-5 & MNT-2L1 to MNT-2L3.

3.3 BET Analysis:

The BET surface area analyzer was used to examine the surface area, pore volume, and pore diameter of UDT, MNT-2, and MNT-2L2. Nitrogen adsorption-desorption experiments indicated that MNT-2L2 displayed H_2-type hysteresis loops, a characteristic feature of mesoporous materials, along with Type-IV isotherms, as shown in Fig. 3a. The pore size distribution was assessed using the Barrett-Joyner-Halenda (BJH) method.

Among the analyzed samples, MNT-2L2 exhibited the highest surface area of 182.79 m^2/g, followed by MNT-2 with 102.34 m^2/g, as depicted in the adsorption-desorption isotherms (Fig. 4a). The corresponding pore diameters for MNT-2L2, MNT-2, and UDT were 30 nm, 35 nm, and 40 nm, respectively, confirming their classification as mesoporous materials (Fig. 4). The presence of an H_2 hysteresis loop further validates the existence of mesopores with a uniform pore structure, which enhances the material's adsorption and catalytic properties.

A clear trend was observed, where a reduction in particle size resulted in an increased surface area. This direct relationship between surface area and

Journal of Chemical Health Risks
www.jchr.org
JCHR (2025) 15 (03), 1161-1190 | ISSN: 2251-6719

photocatalytic efficiency highlights the enhanced performance of Mg-Ni co-doped TiO_2 nanoparticles over pristine TiO_2 (UDT). These results indicate that the co-doped catalysts exhibit superior textural properties, which play a crucial role in their improved photocatalytic activity [26].

Table-4. Catalysts surface area, pore volume and pore size

Catalyst code	Surface-area(m^2/g)	Pore-Volume(cm^3/g)	Pore-size (nm)
UDT	61.89	0.21	41
MNT-2	102.34	0.48	35
MNT-2C2	182.79	0.61	30

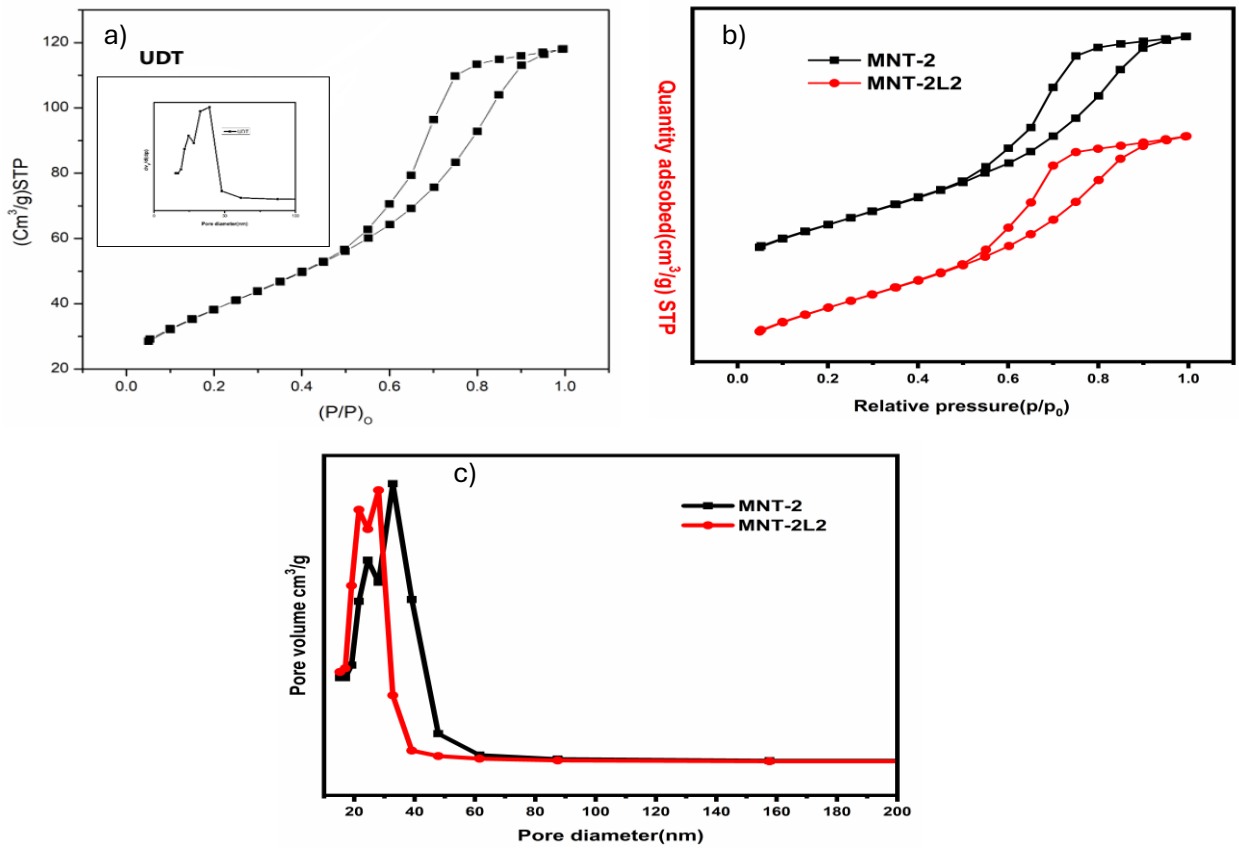

Fig.4 Shows a) UDT adsorption and desorption and pore size b) N2 adsorption & desorption isotherm of MNT-2 & MNT-2L2 c) BJH- Pore size distribution curves of MNT-2 & MNT-2L2

3.4 HRTEM analysis:

Figures 5 & 6 illustrate the HRTEM images of UDT, MNT-2, and MNT-2L2. The MNT-2 exhibited a smaller particle size in comparison to UDT. This is due to the Presence of Mg^{+2},Ni^{+2},Ti^{+4} due to these ions particles attain more positive charge, which exhibits grain strain leads to shrinkage of particle, ultimately grain strain increases particle size decreases, [27]. Further MNT-2L2 demonstrates notably reduced particle size and decreased

Journal of Chemical Health Risks
www.jchr.org
JCHR (2025) 15 (03), 1161-1190 | ISSN: 2251-6719

agglomeration, attributed to the encapsulation of capping agent (lemon juice) [28]. The HRTEM images indicate that Mg-Ni doped TiO_2 comprises nano-crystals exhibiting the anatase phase, which are oriented randomly. The interplanar d-spacing of the particles measured 0.386 nm, which corresponds to the anatase plane. The presence of a crystalline anatase phase is further indicated by the observation of concentric rings, serving as additional evidence for its existence. Figure 5 displays the images of MNT-2L2, including selected area electron diffraction (SAED), lattice fringes, and histogram respectively. The Gaussian fitting method was employed, revealing that the histogram of particle size distribution indicated an average particle size of 10.1 nm for MNT-2L2, 12 nm for MNT-2, and 15.2 nm for UDT. The average particle size was determined using ImageJ software, which enabled precise measurement and analysis of the HRTEM images.

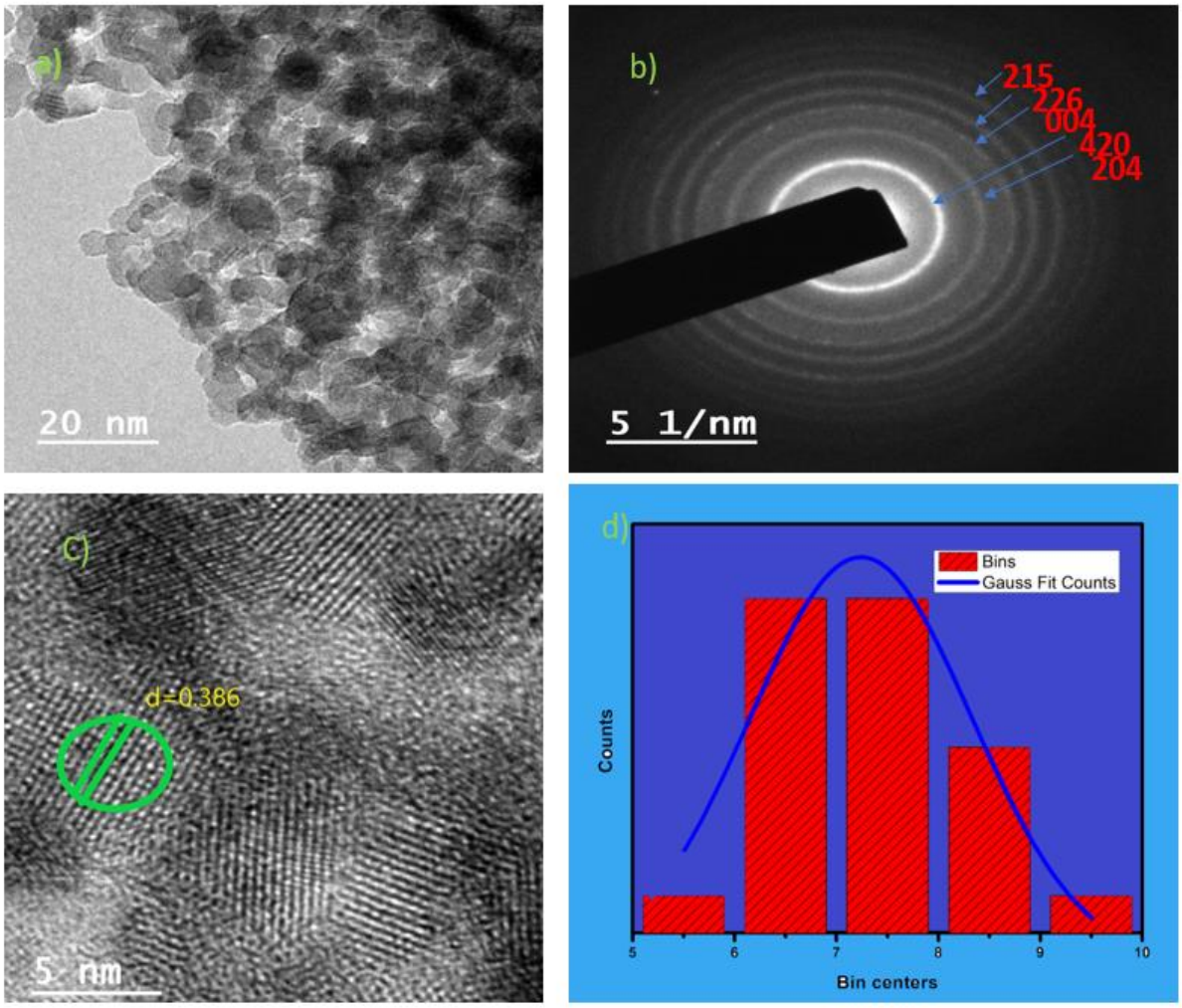

Fig.5 TEM micrograph a) MNT-2L2 b)SAED Pattern of MNT-2L2 c) HRTEM image MNT-2L2 and Lattice fringes d)Histogram of MNT-2L2

Journal of Chemical Health Risks
www.jchr.org
JCHR (2025) 15 (03), 1161-1190 | ISSN: 2251-6719

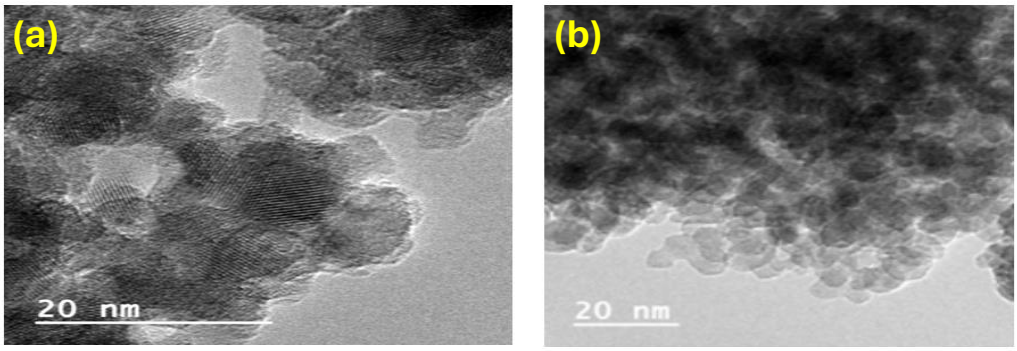

Fig. 6. Shows TEM micrograph of a) MNT-2 b) Undoped TiO_2

3.5 Photoluminescence

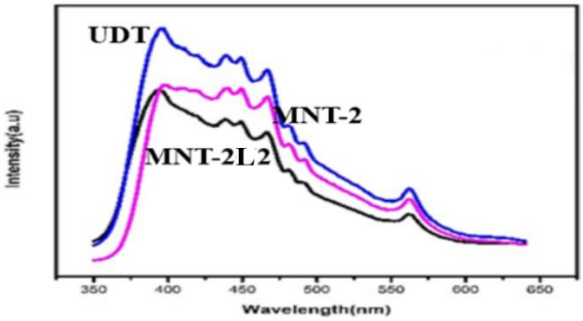

Fig.7 Shows PL spectra for MNT-2L2 for UDT,MNT-2,MNT-2L2.

Photoluminescence spectra (PLS) are essential for studying semiconductors, providing insights into electron-hole dynamics by analyzing charge carrier movement, diffusion, and confinement efficiency. A reduction in photoluminescence intensity typically suggests that the lifetimes of photogenerated carriers are extended and that recombination rates are diminished. Fig.8.a) presents the PL spectra of the synthesized semiconductor catalyst UDT, MNT2, MNT-2L2. The observation of a wide emission peak for UDT within the wavelength range of 380 to 400 nm in the spectrum suggests that the photoexcited electrons are undergoing recombination and moving from the conduction band to the valence band. The observed emission peaks at wavelengths of 437nm, 448nm, and 466nm can be linked to shallow trap states situated close to the emission wavelength of the absorption band. The decrease in PL intensity of emission peaks of these catalysts (MNT2, MNT-2L2) observed very low intensity emission peaks due to doping of Mg^{2+} and Ni^{2+} ions, where Ni^{2+} can be attributed to a reduction in the radiative recombination rate that occurs after photoexcitation. The decrease in radiative recombination of the electron-hole pair takes place as the excited electron transitions from the conduction band of TiO_2 to the metal ion, where it is subsequently absorbed by O_2 on the surface of the metal ion. The presence of metal ions on the surface of TiO_2 creates an additional Schottky barrier that aids in the capture of electrons. Additionally, the metal defects could function as distinct energy centers,

Journal of Chemical Health Risks
www.jchr.org
JCHR (2025) 15 (03), 1161-1190 | ISSN: 2251-6719

facilitating the trapping of excited electrons by O_2. The presence of metal ions facilitates the transfer of charge carriers, leading to a decrease in the overall PL intensity. The observation of emission peaks at wavelengths of 482 nm and 491 nm indicates the presence of deep trap states. The MNT-2C2 sample exhibits an increased rate of dye degradation or photocatalysis due to the reduction of electron-hole recombination [29].

3.6 Impedance

Figure 8b depicts the real and imaginary parts of impedance using a Nyquist plot. The MNT-2L2 data has the lowest impedance values for both real and imaginary components. This implies that this catalyst has the lowest resistance and possibly the least capacitive or inductive effects. MNT-2 has greater impedance values than MNT-2L2, but is still much lower than UDT, indicating moderate resistance characteristics. The UDT has the highest impedance values in both real and imaginary directions, indicating that this sample has the largest resistance and likely the most reactance. The increased impedance is the result of a combination of high resistance. The MNT-2L2 sample has higher photocatalysis due to the lower impedance value. To gain deeper insight into the effects of Mg and Ni doping in TiO_2, electrochemical impedance measurements were conducted at a fixed frequency of 1 kHz while varying the applied voltage from 3 V to -0.5 V. The experiments were performed in an electrolyte solution containing 2 mM $K_3[Fe(CN)_6]$ and 0.1M KCl. Using the Mott–Schottky equation, the space-charge capacitance (Csc) at the semiconductor/electrolyte interface was determined from the impedance data. The relationship between $1/Csc^2$ and potential for the samples UDT, MNT-2, and MNT-2L2 is illustrated in Fig. 8(b), where the positive slopes observed in the Mott–Schottky plots indicate that the samples exhibit n-type behavior. The flat-band potential (Efb), which corresponds to the voltage required to eliminate band bending at the semiconductor/electrolyte interface, was determined to be -0.08 V, -0.12 V, and -0.19 V for Undoped TiO_2, MNT-2, and MNT-2L2, respectively, against Ag/AgCl [30,48]. The supplementary data includes the remaining electrochemical analysis experiments (CV, LSV, CA, CC).

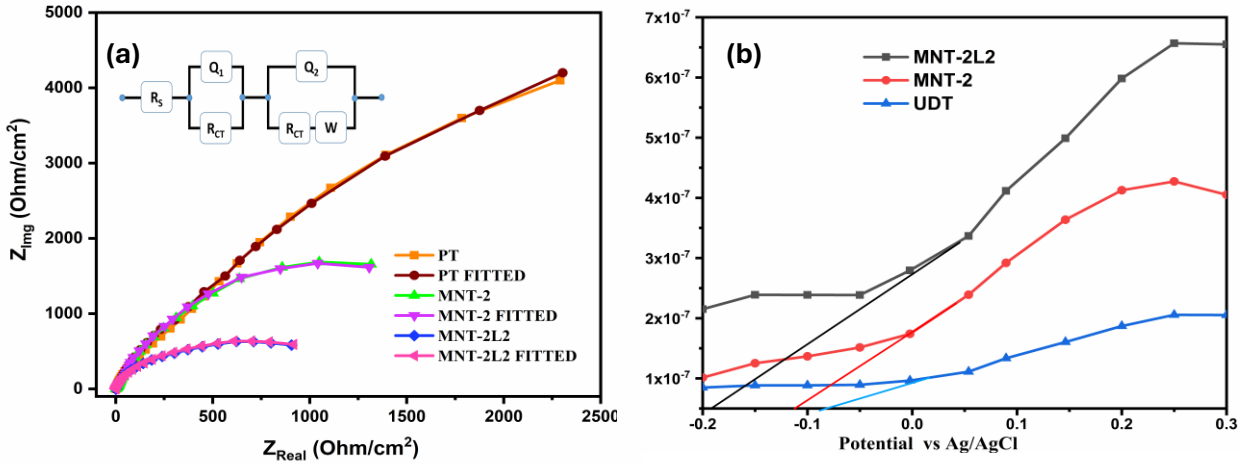

Fig.8 Shows a) Nyquist plot of UDT, MNT-2, MNT-2L2 b) Mott–Schottky plots for UDT, MNT-2 and MNT-2L2 samples

Journal of Chemical Health Risks
www.jchr.org
JCHR (2025) 15 (03), 1161-1190 | ISSN: 2251-6719

3.7 VB-XPS analysis

To acquire a better understanding of the band gap narrowing process in doped materials, a valence band XPS analysis was performed, as shown in Fig.9. It clearly demonstrated that the presence of dopants reduces the band gap. The VB width of MNT-2L2 indicates a higher charge movement capacity in Mg, Ni co-doped TiO_2. The expected maximum energy of the MNT-2L2 valence band was 2.04 eV, with a band tail at around 1.74 eV. Fig.9. MNT-2C2 has an optical band gap energy of 2.50 eV. The conduction band minimum would be around -0.46 eV. TiO2 possesses valence band maxima and conduction band minima, which help to reduce its band gap. The reduction in bandgap demonstrated greater photocatalysis.

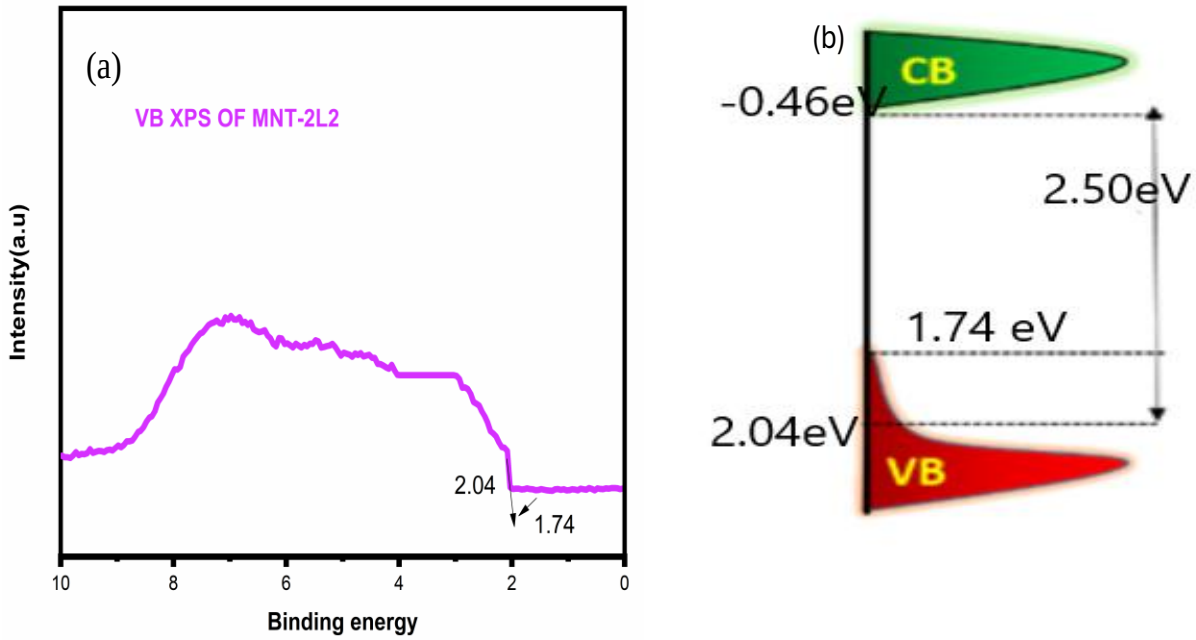

Fig.9 a) VB-XPS of MNT-2L2 b) schematic diagram of the DOS of MNT-2L2

3.8 XPS data Analysis:

X-ray photoelectron spectroscopy, can be used determined the oxidation states and chemical composition of the elements in the MNT-2L2, as illustrated in Fig.10.a. The survey spectrum of the catalyst is presented, featuring the typical elements of Carbon, Oxygen, Magnesium, Nickel, and Titanium. Figures 10.b to f illustrate the magnified spectra of Ti^{4+}, Mg^{2+}, Ni^{2+}, and O^{2-}. The binding energies of titanium are measured at 465.21 eV and 459.13 eV, respectively. This is indicated by doublet peaks at Ti 2p1/2 and Ti 2p3/2, as shown in the spectra in Figure 10.b. The splitting energy of 6.08 eV between these two peaks suggests the presence of the Ti^{4+} ion. When examining doped versus undoped TiO_2, it is observed that undoped TiO_2 exhibits lower Ti^{4+} binding energies for Ti 2p1/2 and Ti 2P3/2, recorded at 462.81 eV and 458.22 eV, respectively. The peak energy splitting difference is noted to be 4.59 eV [31-33]. The introduction of Mg^{2+} and Ni^{2+} into the TiO_2 lattice may result in minimal alterations to the TiO_2 structure. Fig. 10.e spectrum indicates that the binding energies for Mg and MgO are observed at 1303.58 eV and 1304.28 eV, respectively, with a splitting energy of 0.7

Journal of Chemical Health Risks
www.jchr.org
JCHR (2025) 15 (03), 1161-1190 | ISSN: 2251-6719

eV. It has been demonstrated that Mg can be effectively incorporated into the TiO_2 lattice [34]. Figure 10.f spectrum indicates that the Ni 2p region displays four peaks, which are identified as Ni^{2+}. The peaks observed at 881.5 and 874.5 eV, are attributed to Ni 2p3/2 and Ni 2p1/2, respectively. Figure 10.d illustrates that the two peaks observed in the O1s spectra, which correspond to lattice oxygen (Ti-O-Ti) and adsorbed oxygen on the surface (Ti-OH and O^{2-}), are located at 529.46 eV and 530.41 eV, respectively, resulting in a peak energy splitting difference of 0.95 eV [35-37].

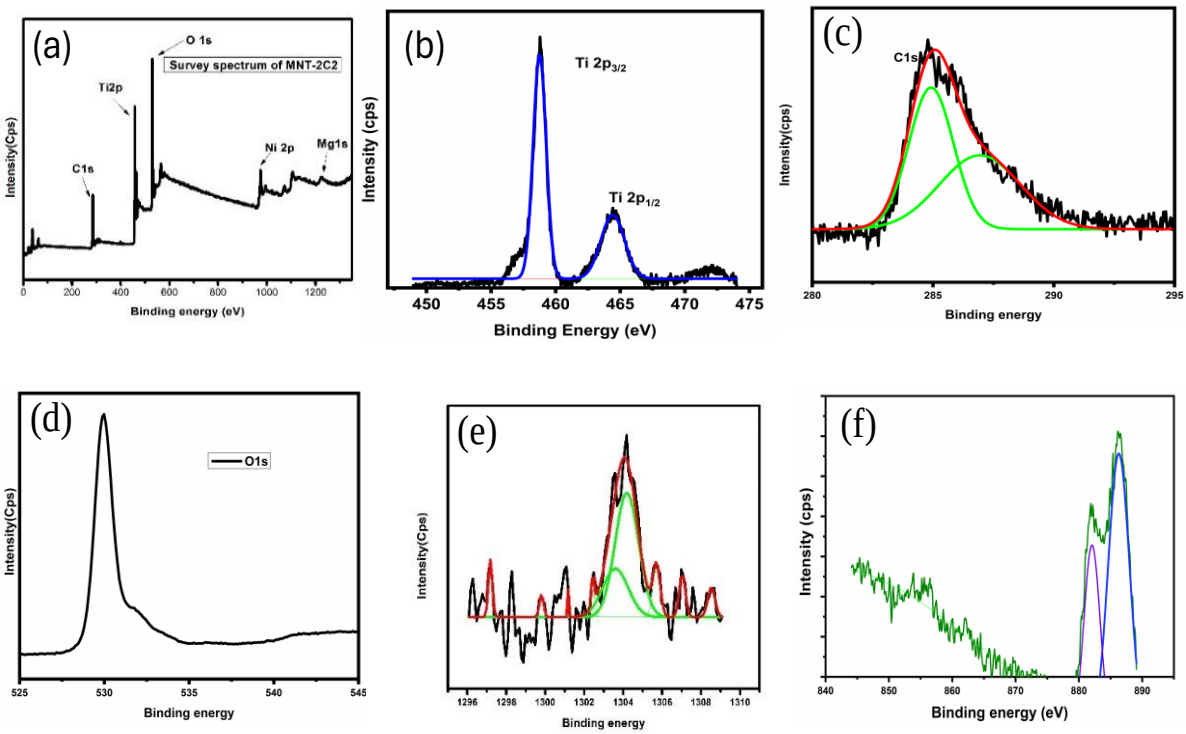

Fig.10 Shows the XPS of a) survey spectrum of MNT-2L2 b) Elevated-Resolution Ti-2p Spectra c) Elevated-Resolution spectra C1s d) Elevated-Resolution spectra O1s e) Mg 1s f) Ni 2p

3.9 XRF Analysis:

A widely employed and dependable method for determining the chemical and qualitative composition of a catalyst is X-ray fluorescence analysis, which entails irradiating the material with high-energy X-ray photons and monitoring the resulting fluorescence emitted by the material [38]. The experimental results indicated that the weight percentage of the doped element and the amount of doping within the TiO_2 lattice were nearly the same. Table-5 included an insert figure for the MNT-2L2 catalyst utilized in Fig.11.

Journal of Chemical Health Risks
www.jchr.org
JCHR (2025) 15 (03), 1161-1190 | ISSN: 2251-6719

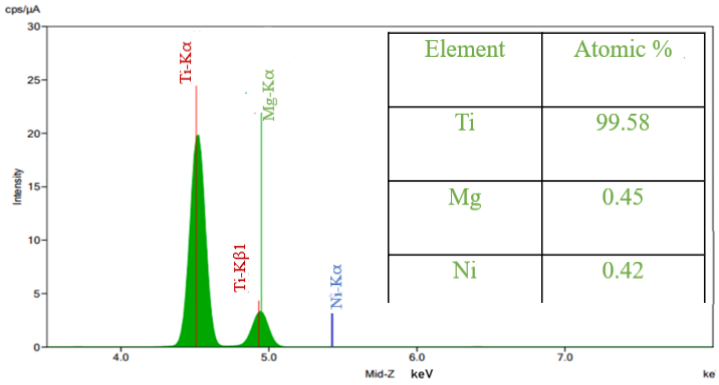

Fig. 11. XRF analysis of MNT-2L2 catalyst & Photocatalysis of the catalysts (evaluation of catalytic efficiency of the catalyst).

4. FESEM Analysis:

The morphological characteristics along with the composition of the catalyst MNT-2L2 were analyzed using an EDX analyzer and a FESEM; the corresponding images are presented in Fig. 12.a, to f. The SEM images of the MNT-2L2 catalysts reveal a rough morphology and a spherical shape, indicating that Mg and Ni were successfully incorporated into the TiO_2 lattice [39]. The chemical composition of the produced catalyst was determined using EDX within the binding energy range of 0 to 10 keV. The co-doped TiO_2 (MNT-2L2) catalyst exhibits signals for Mg, Ni, Ti, and O. The experimental results yield values that closely align with the actual weight percentage doped as dopants in the catalyst MNT-2L2.

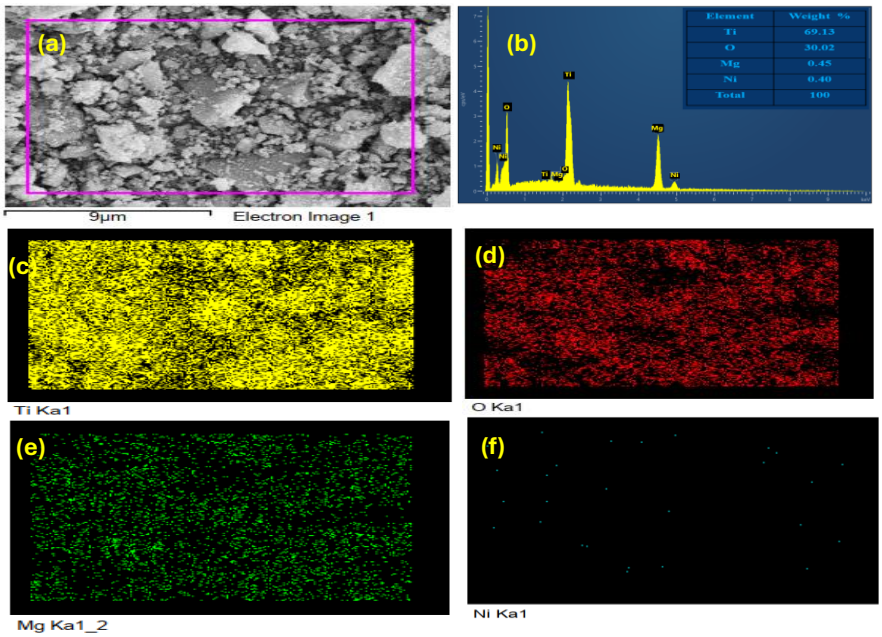

Fig.12 a) FESEM image of MNT-2L2 b) FESEM-EDX of MNT-2L2 c),d),e) &f) FESEM images of Titanium, Oxygen, Magnesium & Nickel.

Journal of Chemical Health Risks
www.jchr.org
JCHR (2025) 15 (03), 1161-1190 | ISSN: 2251-6719

4.1 FTIR Data Analysis:

Figure 13 presents the FTIR spectra for both the undoped and doped (UDT, MNT-2, MNT-2L2) nanoparticles. The spectra exhibited a broad absorption band within the range of 4000 to 3000 cm^{-1}, suggesting the presence of surface hydroxyl groups (Ti-OH stretching vibration). Additionally, the catalyst exhibited an absorption peak at approximately 1658 cm^{-1}, which can be attributed to the bending vibration of H_2O molecules (H-OH). Furthermore, Characteristic absorbance peaks at 497 cm^{-1} indicate the stretching vibrations of Ti-O-Ti in UDT, which was Shifted towards higher wave number of 500 to 565cm^{-1}[Yao, Y et al. 2013]. This frequency shift is the result of Magnesium and Nickel successfully co-doping the TiO_2 lattice as a substitutional, Mg-O-Ti, Ni-O-Ti patterns. The integration of Mg and Ni into the TiO_2 lattice is responsible for the shift in some peaks and the extra peaks. According to the interpretation of the results shown in Fig.13 indicates that Mg and Ni have been effectively incorporated into the TiO_2 lattice [41-42].

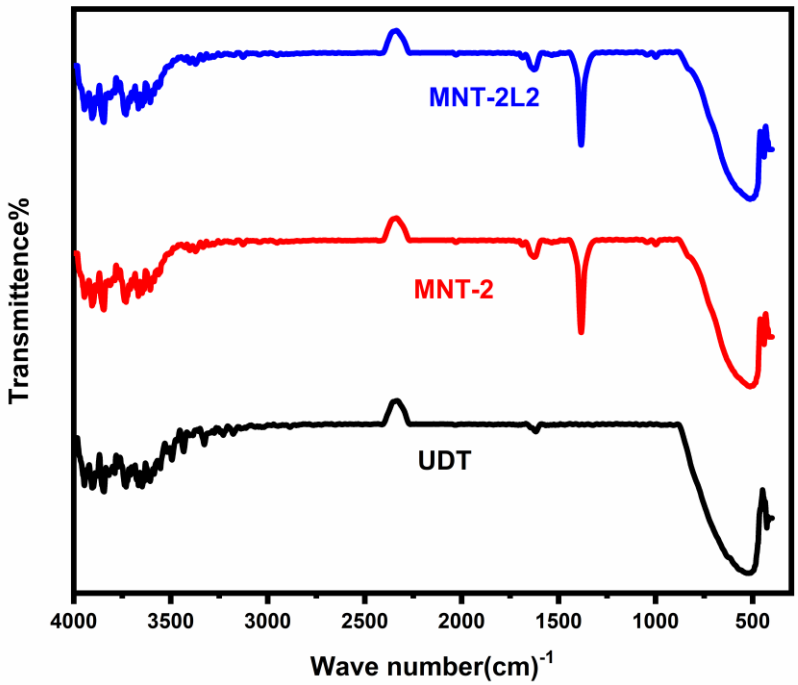

Fig.13 shows FTIR spectra of UDT, MNT-2and MNT-2L2

5. Study on the Applications of the catalyst for degradation of Acid red 249 dye:

The photocatalytic degradation capacity of each co-doped and undoped catalyst was evaluated by altering reaction parameters such as dopant concentration, pH effect, catalyst dosage, and inception dye concentration, specifically focusing on the degradation of Acid red 249 dye. Prior to standardizing the reaction conditions, experiments were conducted to investigate the interdependence of parameters such as light and catalyst.

Trail-1 photolysis: A 150 ml Pyrex glass vessel was filled with the required concentration of Acid red dye solution,

Journal of Chemical Health Risks
www.jchr.org
JCHR (2025) 15 (03), 1161-1190 | ISSN: 2251-6719

which was then exposed to visible light for 60 minutes. The absorbance was measured at λ max 540 nm. The observation reveals that the absorbance values remain unchanged, suggested that dye degradation does not depend on light only.

Trail-2 Adsorption experiment, a 150 ml beaker was prepared with a specific quantity of dye and catalyst. The mixture was stirred for 60 minutes under conditions devoid of light. Subsequently, the absorbance at the λ max value was recorded. The dye solution exhibited a minor variation in absorbance. This may arise from the establishment of an adsorption-desorption equilibrium between the catalyst surface and the dye molecules.

Trail-3 Photocatalysis experiment, a 150 ml beaker taken with a specific quantity catalyst and add small quantity of acid or base to maintain required pH, later add dye solution and then subjected to visible light for a duration of 60 minutes with continues stirring. At different intervals of time collect 5ml aliquots from the reaction mixture and measure the absorbance at same λ_{max}. A significant decrease in the absorbance values has been observed. The findings indicated that the catalyst was energized by light, resulting in the formation of hydroxyl radicals that facilitated the breakdown of the absorbed dye molecules. The findings indicate a relationship between light and the catalyst illustrated in Fig.14a.

To attain the best conditions, additional factors like the impact of pH, the influence of catalyst dosage, and dye concentrations were examined to reach the highest degradation of acid red dye. During the experiments, one parameter was altered while the other parameters of each reaction remained constant.

5.1 Effect of dopants concentration on Catalysis:

Using co-doped magnesium and nickel catalysts at different dopant concentrations, photocatalytic degradation of acid red 249 dye was conducted under visible light while maintaining constant pH-4, 0.15g catalyst weight, and acid red dye concentration of 5mg/L. Absorbance was measured. Displayed in Fig.14.e. The figure indicates that MNT-2L2 demonstrates superior efficiency compared to the other catalysts, including Undoped TiO_2. This could be attributed to the small particle size of 10.1 nm and a high surface area of 182.79 m^2/g.

5.2 pH effect:

Catalysis is a surface phenomenon, where the charge of the catalyst's surface plays a crucial role. In this study, the variation of the pH of the solution in the reaction was examined by altering the pH while maintaining another parameters constant. To provide detailed information on the effect of pH on the photocatalytic activity of MNT-2L2, the pH was varied from 2 to 6 (pH 2, 3, 4, 5, 6) as shown in Fig. 14.d, while maintaining optimum conditions (catalyst dosage of 0.15 g and dye dosage of 5 mg/L). The photocatalytic degradation at each pH effect was determined by taking a 5 ml aliquot of the sample from the reaction mixture, followed by measuring the absorbance. Results from the experiment indicate that the dye exhibited a more rapid degradation at pH 4 [47].

The catalyst surface is expected to exhibit a positive charge at this pH, suggesting that the solution's pH exceeds the pKa values of the Acid red 249 dye. This leads to a decrease in dye particles by enhancing the electrostatic interaction between a growing number of negatively charged Acid Red dye particles and the positively charged surface of the catalyst [43,44].

Journal of Chemical Health Risks
www.jchr.org
JCHR (2025) 15 (03), 1161-1190 | ISSN: 2251-6719

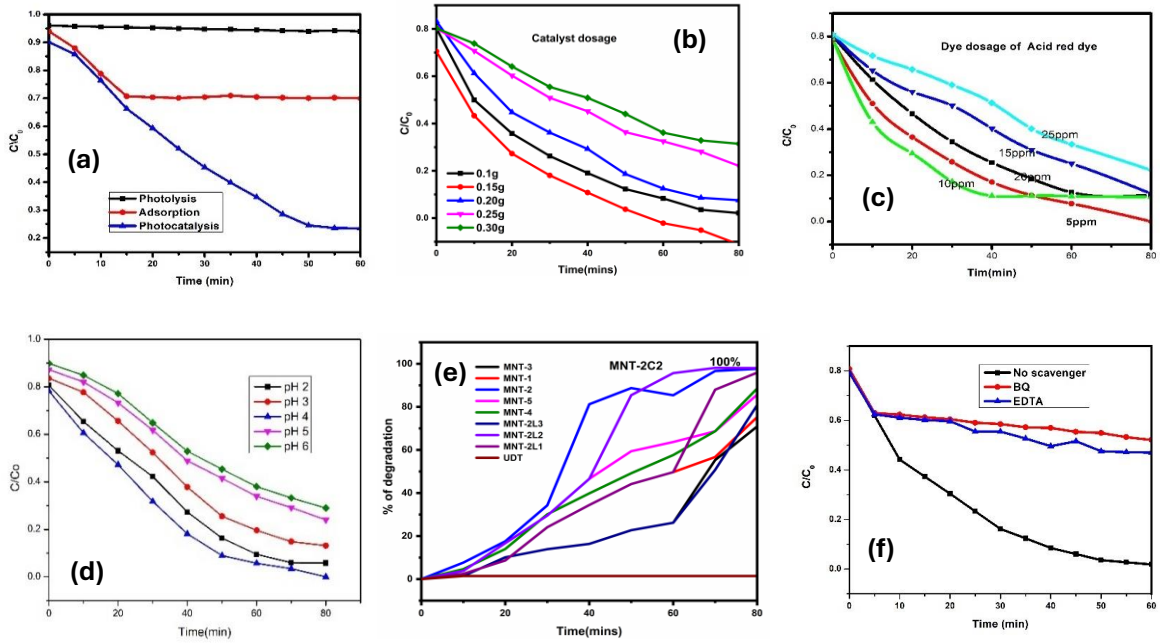

Fig.14 Shows a) Photolysis, adsorption-desorption Equilibrium and Acid red 249 degradation b) Photocatalysis by using different catalyst dosages c) Photocatalysis of different Dye dosage d) Photocatalysis using different pH e) Photocatalysis of different Photocatalysts f) Scavenger effect for electron /hole or $O_2^{\cdot-}$.

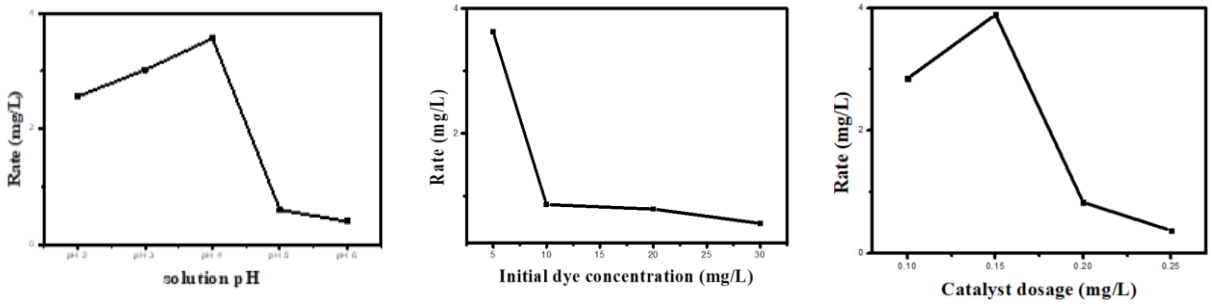

Fig.15 Shows the Rate graph.

5.3 Study on effect of Catalyst dosage:
The breakdown of the Acid red 249 dye was conducted using the MNT-2L2 catalyst at different dosages. By enhancing the catalyst dosage rate of degradation increases up to 0.15 further increase the catalyst dosage rate of catalysis decreases. This concentration demonstrated a greater rate of abatement compared to other concentrations. The presence of catalyst particles for a significant quantity of dye particles was limited by catalyst dosages below 0.15 grams. Consequently, the rate of degrading response was extended. Nonetheless, it increases to 0.15 grams, after which it decreases and ultimately stabilizes due to turbidity, which subsequently diminishes and restricts the penetration of visible light necessary to activate the catalyst particles [45].

Journal of Chemical Health Risks
www.jchr.org
JCHR (2025) 15 (03), 1161-1190 | ISSN: 2251-6719

5.4 Study on concentration variations on Acid red 249 dye:

The amount of Acid red dye influences its degradation rate. This can be achieved by varying the dye concentrations while keeping the other parameters constant. The results of the experiment are presented in Figure 14.c. The figure clearly demonstrates that the concentration of the dye plays a significant role in the photocatalytic abatement rate of Acid red dye in aqueous media. By adjusting its concentration to 5 mg/L, 10 mg/L, 15 mg/L, 20 mg/L, and 25 mg/L at pH-4, the effect of Acid dye fixation on the photocatalytic activity of the MNT-2L2 catalyst was determined. The reaction data presented in Fig.14.c indicates that the maximum degradation rate was achieved in 80 minutes with a dye concentration of 5 mg/L. Even if the amount of dye particles increases while the number of catalyst particles remains the same, the rate of degradation will decrease. As dye concentration increases at a fixed catalyst dosage, catalytic efficiency decreases due to the blanket effect, which limits surface activity. With constant catalyst levels, reactive species (OH•) generation cannot match the excess dye molecules [45,46]. Optimal photocatalytic degradation was observed with 5 ppm Acid Red dye, 0.15 g MNT-2C2 catalyst, at pH 4, achieving significant breakdown within 80 minutes.

5.5 Overall optimum conditions for complete abatement of Acid red dye249:

The MNT-2L2 catalyst was identified as the most efficient catalyst for complete degradation within 80 minutes under specific optimized reaction conditions: a catalyst dosage of 0.15 grams, a pH of 4, and an initial dye concentration of 5 mg/L. Figure 14 presents additional reaction parameters and optimal conditions. The findings on degradation were analyzed in relation to those documented in existing literature, which involved the degradation of the same pollutants through various catalysts. The results of the comparison are presented in Table 6.

Degradation Mechanism of MNT-2L2 catalyst:

Mg-Ni (TiO_2) +hν	⟶	Mg-Ni(TiO_2)Vh^++ Mg-Ni(TiO_2)C e^-	Electron and hole formation
Mg-Ni(TiO_2)Vh^++H_2o	⟶	Mg-Ni(TiO_2)+ ^-OH+ H^+	OH^- and H^+ generated
Mg-Ni(TiO_2) Vh^++OH^-	⟶	Mg-Ni(TiO_2)+ $^·OH$	$^·OH$ produced
Mg-Ni(TiO_2)C e^-+O_2	⟶	Mg-Ni(TiO_2)+$O_2^{·-}$	Super oxide radical formation
Mg-Ni(TiO_2)C e^-+O_2^- +H_2O	⟶	Mg-Ni(TiO_2)+$HO_2^·$+OH^-	$HO_2^·$,OH^- formation
Mg-Ni(TiO_2) C e^- +$HO_2^·$+H^+	⟶	Mg-Ni(TiO_2)+H_2O_2	Hydrogen peroxide formation
Mg-Ni(TiO_2) C e^- +H_2O_2	⟶	Mg-Ni(TiO_2)+$^·OH$+OH^-	Hydroxyl radical and hydroxyl ion produced
Acid red 249 pollutant	⟶	Degradation products	(CO_2 ,H_2O)

Journal of Chemical Health Risks
www.jchr.org
JCHR (2025) 15 (03), 1161-1190 | ISSN: 2251-6719

Vibrio cholerae (MTCC-3906)	→	Degradation of protein coat	Bacteria killed.

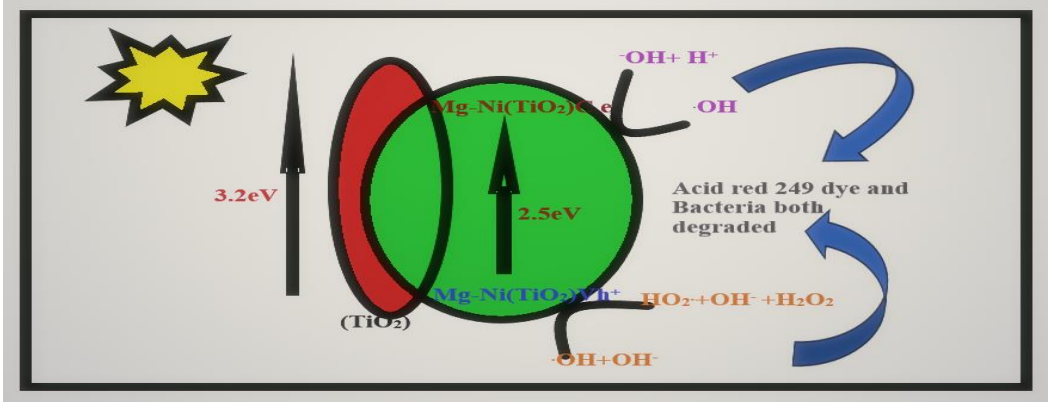

Fig.16 Graphical Mechanism of MNT-2L2

Table-6. Photocatalyst

S.No	Photocatalyst used	Organic pollutant	Time for degradation	Degradation efficiency %	Reference
1.	ZnO Composites	Acid red 249 dye	120 mins	93.7%	[44]
2.	Bacillus flexus(microbe)	Acid red 249 dye	10 hrs	100%	[52]
3.	Exfoliated graphite and H_2O_2	Acid red 249 dye	180 mins	85.69%	[53]
4.	ZnO/Graphene oxide	Acid red 249 dye	120 mins	94.8%	[54]
5.	Mg-Ni doped Tio2	Acid red 249 dye	80 mins	100%	Present work

The current catalyst demonstrates 100% catalysis in 80 minutes when compared to all other catalysts stated for the degradation of acid red dye.

5.6 Recyclability of the catalyst:
The stability of a catalyst in the catalytic process is crucial for its repeated use. In industrial applications, catalysts are utilized in continuous processes, where they may experience erosion, particularly under aggressive acidic conditions. Therefore, testing and evaluating catalyst stability is essential to ensure its long-term effectiveness in industrial operations.

To assess stability, evaluations were conducted under optimized conditions. After five cycles, no significant differences were observed before and after recyclability, as confirmed by XRD and SEM analyses [49]. These results indicate that the catalyst maintains good stability even after multiple-cycles. Throughout five cycles of photocatalysis, the reaction rate exhibits minimal changes. The solid catalyst was recovered from the Acid red dye solution through a series of washings with ultrapure deionized water, followed by centrifugation at 3500 RPM for 10 minutes, and finally dried in an oven. After each

Journal of Chemical Health Risks
www.jchr.org
JCHR (2025) 15 (03), 1161-1190 | ISSN: 2251-6719

cycle, a new solution of Acid red dye and the dried catalyst were utilized for the photocatalytic degradation process. The same procedure was conducted for up to five more cycles utilizing the same catalyst. Every parameter, such as the catalyst to Acid red dye fixation ratio, the volume of solution utilized, visible radiation flux, distance from the light source, and the pH of the solution, was meticulously calibrated for each trial. Figure 17.a illustrates the MNT-2L2 test performed over five cycles. Strong evidence shows that the reaction rate and catalyst activity largely stayed consistent even after multiple cycles of recycling the catalyst sample. XRD and SEM analysis were performed following the recycling process of acid red dye 249 degradation. The X-ray diffraction (XRD) and SEM, indicate that there is no substantial difference between the recycled catalyst and the synthesized catalyst and depicted in Figure 17.b and c.

5.7 Scavenger test for Reactive species (h^+, O^{2-}, and $OH^{\cdot}$):

To evaluate the significant reactive species (h^+, O^{2-} (Superoxide) scavenger tests were conducted. The hydroxyl radical was involved in the photocatalytic process and was detected using a scavenger reagent test. Three samples were prepared for that purpose.

In the initial sample, the identification of the hole (h+) was conducted by incorporating 1M disodium salt of EDTA after a duration of 5-10 minutes, followed by exposure to visible light, and the absorbance was subsequently measured up to 25 min. After a period, the absorbance reaches a constant value. The results obtained suggest that a formation hole exists, and the size of the hole stabilized through the EDTA reaction. Figure 14.f illustrates the reaction between hole and EDTA point. To identify the superoxide radical (O^{2-}), a second sample was taken, and Benzoquinone reagent was added to the reaction solution after 10-15 minutes and exposed to visible light, resulting in diminished photocatalytic degradation of Acid red 249 dye. The analysis results are presented in Fig. 14, indicating that the O^{2-} species plays a specific role in the Acid red dye.

The presence of $OH^{\cdot}$ in the photocatalytic degradation reaction was identified through the photoluminescence (PL) technique. After a duration of 15-20 minutes, coumarin was introduced into the solution, leading to the formation of 7-hydroxy coumarin because of the attack by hydroxyl radicals. The conversion process is determined by the fluorescence intensity at 450nm, as outlined in Figure 14. d. The photocatalytic process resulted in the generation of a substantial amount of OH radicals, which interacted with coumarin to produce 7-hydroxycoumarin, illustrated in figure 14.f as a pronounced peak at 450 nm. At 0 minutes, there was no significant absorption peak observed for the degradation of the sample when light was not present. These results demonstrate that hydroxyl radicals are generated on the surface of MNT-2L2 exclusively during the illumination phase. The PL instrumental analysis data indicates that the synthesized MNT-2L2 catalyst produces a substantial amount of OH radicals during photocatalytic reaction.

Journal of Chemical Health Risks
www.jchr.org
JCHR (2025) 15 (03), 1161-1190 | ISSN: 2251-6719

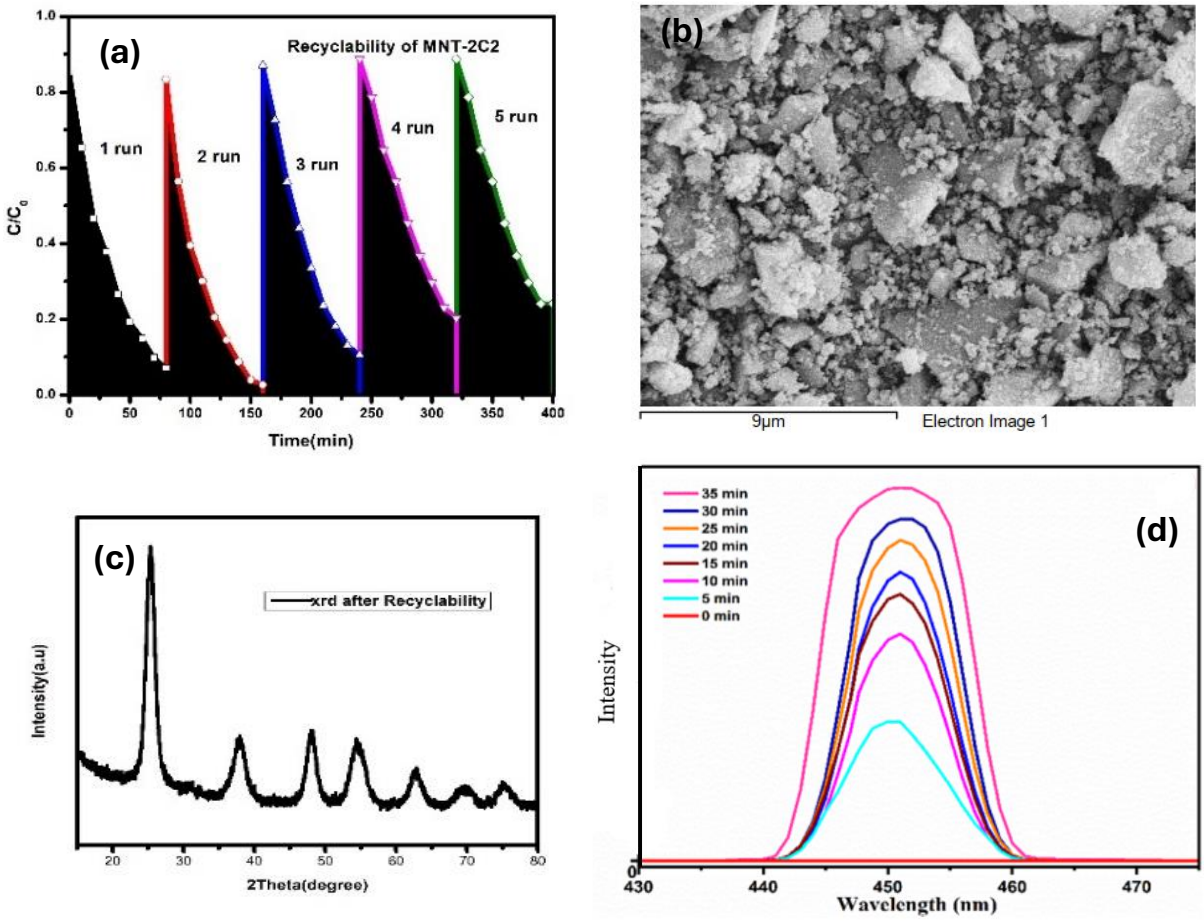

Fig 17. a) Recyclability of photocatalyst MNT-2L2 b) SEM image of MNT-2L2 after recyclability c) XRD after recyclability d) Photoluminesence spectra of OH radical scavenger

6. Antibacterial activity:

This study evaluated the antibacterial activity of MNT-2L2 nanoparticles against bacteria using the Agar-well diffusion method which is discussed in experimental section 2.4 b. The bacterial strain Vibrio cholerae (MTCC-3906) was subjected to different concentrations 400µg/mL, 600µg/mL and 800µg/mL of MNT-2L2 nanoparticles was filled in designated wells of a petri dish. Chloramphenicol served as a standard antibacterial agent for bacteria and was added to each well. The diameter of the inhibition zone was assessed in triplicate for each catalyst dosage. Presented in Table 7. Fig. 18 illustrates the area where bacterial growth is inhibited at a concentration of 800µg/mL. It demonstrates enhanced performance relative to the other two catalyst dosages. The improved antibacterial effectiveness of MNT-2L2 could be linked to the formation of electron h+ in the valence band of TiO_2, which is stimulated by the visible light irradiation of the catalyst. The presence of electrons and holes can act as oxidants, resulting in the degradation of the protein coat (Glycoprotein) of bacteria and subsequently hindering their growth [50].

Journal of Chemical Health Risks
www.jchr.org
JCHR (2025) 15 (03), 1161-1190 | ISSN: 2251-6719

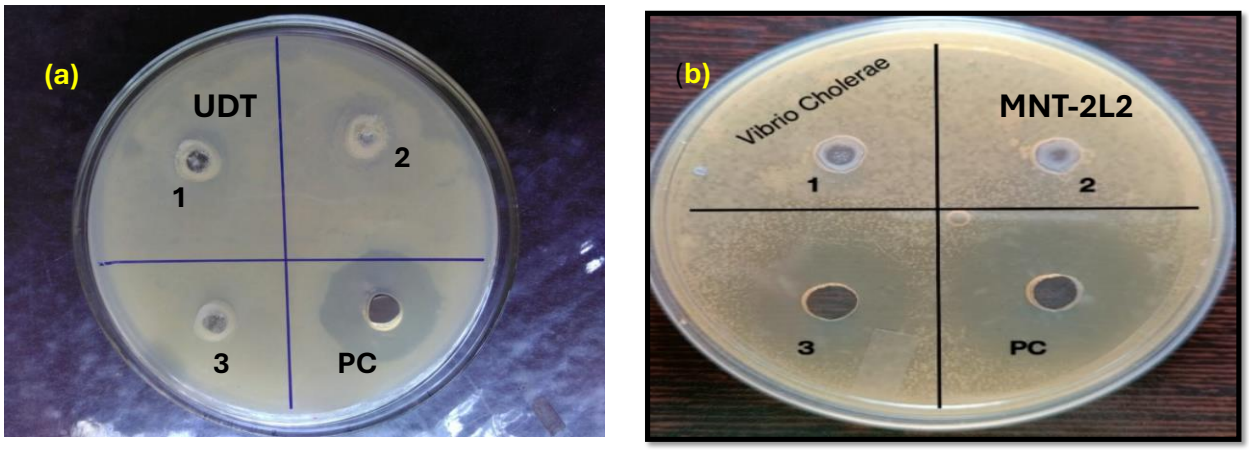

Fig. 18 Shows the inhibition of the catalyst MNT-2L2 for *Vibrio cholerae* (MTCC-3906)

Table.7 Shows the antibacterial results

S. No	Test Organism	Zone of inhibition (mm)			
		Nano catalyst (µg/mL)			
		400	600	800	Standard (Chloramphenicol) 50µg/ml
1	*Vibrio cholerae* (MTCC-3906) ***UDT***	-	-	-	20
2.	*Vibrio cholerae* (MTCC-3906) ***MNT*-2L2**	-	-	23	26

7. Conclusions:

This paper presents a detailed study on the sol-gel synthesis of magnesium and nickel co-doped TiO_2 nanomaterials, utilizing lemon juice as a capping agent. The synthesized catalyst was characterized, confirming the formation of the anatase phase through XRD analysis. UV-VIS DRS measurements demonstrated a reduced band gap of 2.5 eV (MNT2-L2). TEM analysis indicated a decreased particle size of 6.2 nm, while BET analysis revealed a high surface area of 182.79 m^2/g, a pore volume of 0.61 cm^3/g, and a pore size of 30 nm. Based on these characterizations, the catalyst was employed for the photocatalytic degradation of Acid Red 249 dye, achieving complete degradation within 80 minutes under visible light. Additionally, the catalyst exhibited antibacterial activity comparable to standard values.

Acknowledgements:
This research study did not receive any specific grant funding from public, commercial, or nonprofit organizations.

8. References

1. Lu, H., Wang, J., Stoller, M., Wang, T., Bao, Y. and Hao, H., 2016. An overview of nanomaterials for water

and wastewater treatment. *Advances in Materials Science and Engineering*, *2016*(1), p.4964828 http://dx.doi.org/10.1155/2016/4964828.

2. Serpone, N.A.V.E. and Emeline, A.V., 2012. Semiconductor Photocatalysis Past, Present, and Future Outlook. *The journal of physical chemistry letters*, *3*(5), pp.673-677v https://doi.org/10.1021/jz300071j
3. Kapusuz, D., Park, J. and Ozturk, A., 2013. Sol–gel synthesis and photocatalytic activity of B and Zr co-doped TiO2. *Journal of Physics and Chemistry of Solids*, *74*(7), pp.1026-1031http://dx.doi.org/10.1016/j.jpcs.2013.02.022.
4. Botsa, S. M., P, S., Raju, I. M., P, S., Satyanarayana, G., Sambasivam, S., Uppugalla, S., & D, T. (2022). Nanohybrid material of Co–TiO2 and optical performance on methylene blue dye under visible light illumination. *Hybrid Advances*, *1*, 100008. https://doi.org/10.1016/j.hybadv.2022.100008
5. Swati Sood, Ahmad Umar, Surinder Kumar Mehta, Sushil Kumar Kansal,.Highly effective Fe-doped TiO2 nanoparticles photocatalysts for visible-light driven photocatalytic degradation of toxic organic compounds,.Journal of Colloid and Interface Science,Volume 450, 15 july 2015, Pages 213-223,ISSN 0021-9797,https://doi.org/10.1016/j.jcis.2015.03.018.
6. Zhang, P., Liu, C., Yang, X., Chi, M., Zhang, L., Han, Y., Zhang, W., Du, S., & Liu, S. Single-Atom Cu-Doped TiO2 nanorods with modulated surface active sites for superior photocatalytic performance. Journal of Catalysis, (2024). 430, 115321. https://doi.org/10.1016/j.jcat.2024.115321
7. Soundarya, T., Harini, R., Manjunath, K., Udayabhanu, N., Nirmala, B., & Nagaraju, G. (2023). Pt-doped TiO2 nanotubes as photocatalysts and electrocatalysts for enhanced photocatalytic H2 generation, electrochemical sensing, and supercapacitor applications. *International Journal of Hydrogen Energy*, *48*(82), 31855–31874. https://doi.org/10.1016/j.ijhydene.2023.04.289.
8. Li, Y., Walsh, A. G., Li, D., Do, D., Ma, H., Wang, C., Zhang, P., & Zhang, X. (2020). W-Doped TiO2 for photothermocatalytic CO2 reduction. *Nanoscale*, *12*(33), 17245–17252. https://doi.org/10.1039/d0nr03393f
9. Yu, H., Zheng, X., Yin, Z., Tag, F., Fang, B., & Hou, K. (2007). Preparation of Nitrogen-doped TiO2 Nanoparticle Catalyst and Its Catalytic Activity under Visible Light. *Chinese Journal of Chemical Engineering*, *15*(6), 802–807. https://doi.org/10.1016/s1004-9541(08)60006-3
10. Ghumro, S. S., Lal, B., & Pirzada, T. (2022). Visible-Light-Driven Carbon-Doped TiO2-Based Nanocatalysts for Enhanced Activity toward Microbes and Removal of Dye. *ACS Omega*, *7*(5), 4333–4341. https://doi.org/10.1021/acsomega.1c06112
11. Thakur, N., Kumar, A., & Thakur, N. (2023). Tinospora cordifolia and polyvinylpyrrolidone encapsulated dual doped Ni-Cu TiO2 emerging nanocatalyst for the removal of organic dyes from wastewater and its

free radical assay activity. *Hybrid Advances*, *4*, 100086. https://doi.org/10.1016/j.hybadv.2023.100086

12. Talat-Mehrabad, J., Khosravi, M., Modirshahla, N., & Behnajady, M. A. (2015). Synthesis, characterization, and photocatalytic activity of co-doped Ag–, Mg–TiO2-P25 by photodeposition and impregnation methods. *Desalination and Water Treatment*, *57*(22), 10451–10461. https://doi.org/10.1080/19443994.2015.1036780
13. Chen, H., Zhu, W., Zhang, Z., Cai, W., & Zhou, X. (2019). Er and Mg co-doped TiO2 nanorod arrays and improvement of photovoltaic property in perovskite solar cell. *Journal of Alloys and Compounds*, *771*, 649–657. https://doi.org/10.1016/j.jallcom.2018.08.279
14. Sun, T., Fan, J., Liu, E., Liu, L., Wang, Y., Dai, H., Yang, Y., Hou, W., Hu, X., & Jiang, Z. (2012). Fe and Ni co-doped TiO2 nanoparticles prepared by alcohol-thermal method: Application in hydrogen evolution by water splitting under visible light irradiation. *Powder Technology*, *228*, 210–218. https://doi.org/10.1016/j.powtec.2012.05.018
15. Kim, D. H., Lee, K. S., Kim, Y., Chung, Y., & Kim, S. (2005). Photocatalytic Activity of Ni 8 wt%-Doped TiO2 Photocatalyst Synthesized by Mechanical Alloying Under Visible Light. *Journal of the American Ceramic Society*, *89*(2), 515–518. https://doi.org/10.1111/j.1551-2916.2005.00782.x
16. Alim, S. A., Rao, T. S., Miditana, S. R., & Lakshmi, K. V. D. (2020). Efficient and recyclable visible light-active nickel–phosphorus co-doped TiO2 nanocatalysts for the abatement of methylene blue dye. *Journal of Nanostructure in Chemistry*, *10*(3), 211–226. https://doi.org/10.1007/s40097-020-00343-z
17. Athira, K., Merin, K., Raguram, T., & Rajni, K. (2020). Synthesis and characterization of Mg doped TiO2 nanoparticles for photocatalytic applications. *Materials Today Proceedings*, *33*, 2321–2327. https://doi.org/10.1016/j.matpr.2020.04.580
18. Singh, S., Maurya, I. C., Tiwari, A., Srivastava, P., & Bahadur, L. (2022). Green synthesis of TiO2 nanoparticles using Citrus limon juice extract as a bio-capping agent for enhanced performance of dye-sensitized solar cells. *Surfaces and Interfaces*, *28*, 101652. https://doi.org/10.1016/j.surfin.2021.101652
19. Ouerghi, O., Geesi, M.H., Riadi, Y. and Ibnouf, E.O., 2022. Limon-citrus extract as a capping/reducing agent for the synthesis of titanium dioxide nanoparticles: Characterization and antibacterial activity. *Green Chemistry Letters and Reviews*, *15*(3), pp.483-490 https://doi.org/10.1080/17518253.2022.2094205.
20. Peng, Y., Ji, J., Zhao, X., Wan, H., & Chen, D. (2012). Preparation of ZnO nanopowder by a novel ultrasound assisted non-hydrolytic sol–gel process and its application in photocatalytic degradation of C.I. Acid Red 249. *Powder Technology*,

233, 325–330. https://doi.org/10.1016/j.powtec.2012.09.018

21. Díaz, E. (2008). Microbial biodegradation : genomics and molecular biology. In *Caister Academic Press eBooks*. https://ci.nii.ac.jp/ncid/BA84100952
22. Das, S., Sinha, S., Suar, M., Yun, S., Mishra, A., & Tripathy, S. K. (2014). Solar-photocatalytic disinfection of Vibrio cholerae by using Ag@ZnO core–shell structure nanocomposites. *Journal of Photochemistry and Photobiology B Biology*, *142*, 68–76. https://doi.org/10.1016/j.jphotobiol.2014.10.021
23. Chippada, M., Sailaja, B., Rao, T. S., Divya, G., Nayak, S. R., Manogna, B. S., & Jaishree, G. (2023). Structural modification of nano titania by doping with Barium and Copper – Impact on photocatalysis: Applications in degradation of dye and pathogens. *Hybrid Advances*, *3*, 100033. https://doi.org/10.1016/j.hybadv.2023.100033
24. Li, J.C.M.; Feng, C.R.; Rath, B.B. Emission of Dislocations from Grain Boundaries and Its Role in Nanomaterials. *Crystals* **2021**, *11*, 41. https://doi.org/10.3390/cryst11010041
25. Pestryakov, A., Petranovskii, V., Kryazhov, A., Ozhereliev, O., Pfänder, N., & Knop-Gericke, A. (2004). Study of copper nanoparticles formation on supports of different nature by UV–Vis diffuse reflectance spectroscopy. *Chemical Physics Letters*, *385*(3–4), 173–176. https://doi.org/10.1016/j.cplett.2003.12.077
26. Zhou, M., Wei, Z., Qiao, H., Zhu, L., Yang, H., & Xia, T. (2009). Particle size and pore structure Characterization of silver nanoparticles prepared by confined arc plasma. *Journal of Nanomaterials*, *2009*(1). https://doi.org/10.1155/2009/968058
27. Chippada, M., Sailaja, B., Rao, T. S., Divya, G., Nayak, S. R., Manogna, B. S., & Jaishree, G. (2023). Structural modification of nano titania by doping with Barium and Copper – Impact on photocatalysis: Applications in degradation of dye and pathogens. *Hybrid Advances*, *3*, 100033. https://doi.org/10.1016/j.hybadv.2023.100033
28. Ortega, F., Arce, V. B., & Garcia, M. A. (2020). Nanocomposite starch-based films containing silver nanoparticles synthesized with lemon juice as reducing and stabilizing agent. *Carbohydrate Polymers*, *252*, 117208. https://doi.org/10.1016/j.carbpol.2020.117208
29. Liqiang, J., Yichun, Q., Baiqi, W., Shudan, L., Baojiang, J., Libin, Y., Wei, F., Honggang, F., & Jiazhong, S. (2006). Review of photoluminescence performance of nano-sized semiconductor materials and its relationships with photocatalytic activity. *Solar Energy Materials and Solar Cells*, *90*(12), 1773–1787. https://doi.org/10.1016/j.solmat.2005.11.007
30. Chang, B., & Park, S. (2010). Electrochemical Impedance spectroscopy. *Annual Review of Analytical Chemistry*, *3*(1), 207–229.

https://doi.org/10.1146/annurev.anchem.012809.102211

31. Ahmad, A. A., Alakhras, L. A., Al-Bataineh, Q. M., & Telfah, A. (2023). Impact of metal doping on the physical characteristics of anatase titanium dioxide (TiO2) films. *Journal of Materials Science Materials in Electronics*, *34*(20). https://doi.org/10.1007/s10854-023-10948-z
32. Elilarassi, R., & Chandrasekaran, G. (2017). Influence of nickel doping on the structural, optical and magnetic properties of TiO2 diluted magnetic semiconductor nanoparticles prepared by high energy ball-milling technique. *Journal of Materials Science Materials in Electronics*, *28*(19), 14536–14542. https://doi.org/10.1007/s10854-017-7317-4
33. Raguram, T., & Rajni, K. S. (2021b). Effect of Ni doping on the characterization of TiO2 nanoparticles for DSSC applications. *Journal of Materials Science Materials in Electronics*, *32*(13), 18264–18281. https://doi.org/10.1007/s10854-021-06369-5
34. Sood, S., Umar, A., Kumar Mehta, S., Sinha, A., & Kumar Kansal, S. Efficient photocatalytic degradation of brilliant green using Sr-doped TiO2 nanoparticles.CeramicsInternational, 41(3), 3533–3540. (2015, April). https://doi.org/10.1016/j.ceramint.2014.11.010.
35. Singh, M. K., & Mehata, M. S. (2020). Enhanced photoinduced catalytic activity of transition metal ions incorporated TiO2 nanoparticles for degradation of organic dye: Absorption and photoluminescence spectroscopy. *Optical Materials*, *109*, 110309. https://doi.org/10.1016/j.optmat.2020.110309
36. Swathi Padmaja, J., Rao, T. S., Lakshmi, K. D., & Raju, I. M.Fabrication of hetero-structured mesoporous TiO2-SrTiO3 nanocomposite in presence of Gemini surfactant: Characterization and application in catalytic degradation of Acid Orange. Journal of Environmental Chemical Engineering, (2018a). 6(5), 6457–6467. https://doi.org/10.1016/j.jece.2018.09.016
37. Liqiang, J., Xiaojun, S., Weimin, C., Zili, X., Yaoguo, D., & Honggang, F. (2003). The preparation and characterization of nanoparticle TiO2/Ti films and their photocatalytic activity. *Journal of Physics and Chemistry of Solids*, *64*(4), 615–623. https://doi.org/10.1016/s0022-3697(02)00362-1
38. Thambiliyagodage, C., & Mirihana, S. (2021). Photocatalytic activity of Fe and Cu co-doped TiO2 nanoparticles under visible light. *Journal of Sol-Gel Science and Technology*, *99*(1), 109–121. https://doi.org/10.1007/s10971-021-05556-4
39. Hussain, M., Ceccarelli, R., Marchisio, D., Fino, D., Russo, N., & Geobaldo, F. (2009). Synthesis, characterization, and photocatalytic application of novel TiO2 nanoparticles. *Chemical Engineering Journal*, *157*(1), 45–51. https://doi.org/10.1016/j.cej.2009.10.043
40. Kavaliunas, V., Krugly, E., Sriubas, M., Mimura, H., Laukaitis, G., &

Hatanaka, Y. (2020). Influence of Mg, Cu, and Ni Dopants on Amorphous TiO2 Thin Films Photocatalytic Activity. Materials, 13(4), 886. https://doi.org/10.3390/ma13040886

41. Oluigbo, C. J., Xu, Y., Louis, H., Yusuf, A. B., Yaseen, W., Ullah, N., Alagarasan, K. J., Xie, M., Ekpenyong, E. E., & Xie, J. (2021). Controllable fabrication of abundant nickel-nitrogen doped CNT electrocatalyst for robust hydrogen evolution reaction. *Applied Surface Science*, *562*, 150161. https://doi.org/10.1016/j.apsusc.2021.150161
42. Jaishree, G., Divya, G., Rao, T. S., Chippada, M. L. V. P., & Raju, I. M.Biogenic surfactant mediated facile synthesis of visible light sensitized Zn/Mg co-doped TiO2 nanomaterials – a green approach: evaluation of photocatalytic activity by degradation of Amido Black 10B. Sustainable Environment Research, (2022, September 3) . 32(1). https://doi.org/10.1186/s42834-022-00149-4
43. Unnarkat, A., Dharaskar, S., & Kotak, M. (2022). UV/H2O2 Processes for Dye Removal. In *Sustainable textiles* (pp. 147–173). https://doi.org/10.1007/978-981-19-0882-8_5
44. Peng, Y., Ji, J., Zhang, Y., Wan, H., & Chen, D. (2013b). Preparation of poly(m-phenylenediamine)/ZnO composites and their photocatalytic activities for degradation of C.I. acid red 249 under UV and visible light irradiations. *Environmental Progress & Sustainable Energy*, *33*(1), 123–130. https://doi.org/10.1002/ep.11764
45. Chekuri, R. D., & Tirukkovalluri, S. R. (2017b). Synthesis of cobalt doped titania nano material assisted by gemini surfactant: Characterization and application in degradation of Acid Red under visible light irradiation. *South African Journal of Chemical Engineering*, *24*, 183–195. https://doi.org/10.1016/j.sajce.2017.10.001
46. Momeni, M.M., Ghayeb, Y. Synthesis and characterization of iron-doped titania nanohoneycomb and nanoporous semiconductors by electrochemical anodizing method as good visible light active photocatalysts. *J Mater Sci: Mater Electron* **26**, 5509–5517 (2015). https://doi.org/10.1007/s10854-015-3108-y
47. Momeni, M.M., Ahadzadeh, I. & Rahmati, A. Nitrogen, carbon and iron multiple-co doped titanium dioxide nanotubes as a new high-performance photo catalyst. *J Mater Sci: Mater Electron* **27**, 8646–8653 (2016). https://doi.org/10.1007/s10854-016-4885-7
48. Khalaghi, M., Atapour, M., Momeni, M. M., & Karampoor, M. R. (2025). Visible light photocatalytic efficiency and corrosion resistance of Zn, Ni, and Cu-doped TiO2 coatings. *Results in Chemistry*, 102032. https://doi.org/10.1016/j.rechem.2025.102032
49. Ghayeb, Y., Momeni, M.M. Efficient sunlight-driven photocatalytic activity of chromium TiO_2 nanotube nanocomposites prepared by anodizing and chemical bath deposition. *J Mater Sci: Mater Electron* **26**, 5335–5341 (2015). https://doi.org/10.1007/s10854-015-3073-5

50. Ikram, M., Abbas, S., Haider, A., Naz, S., Ahmad, S. O. A., Haider, J., Ul-Hamid, A., Shahzadi, A., Shahzadi, I., & Butt, A. R. Efficient dye degradation, antimicrobial behavior and molecular docking analysis of gold (Au) and cellulose nanocrystals (CNC)-doped strontium oxide nanocomposites. Journal of Nanostructure in Chemistry, (2021)12(5), 933–950. https://doi.org/10.1007/s40097-021-00452-3
51. Pang, Y., Liu, Y., Zhang, X., Gao, M., & Pan, H. (2012). Role of particle size, grain size, microstrain and lattice distortion in improved dehydrogenation properties of the ball-milled Mg(AlH4)2. *International Journal of Hydrogen Energy*, *38*(3), 1460–1468. https://doi.org/10.1016/j.ijhydene.2012.11.006
52. Parmar, N. D., & Shukla, S. R. (2017). Decolorisation by Bacillus flexus of exhausted dyebaths containing CI Acid Red 249 and their reuse for wool dyeing. *Coloration Technology*, *133*(3), 218–222. https://doi.org/10.1111/cote.12270
53. Li, M., Li, J., & Sun, H. (2007). Decolorizing of azo dye Reactive red 24 aqueous solution using exfoliated graphite and H2O2 under ultrasound irradiation. *Ultrasonics Sonochemistry*, *15*(5), 717–723. https://doi.org/10.1016/j.ultsonch.2007.10.001
54. Peng, Y., Ji, J., & Chen, D. (2015). Ultrasound assisted synthesis of ZnO/reduced graphene oxide composites with enhanced photocatalytic activity and anti-photocorrosion. *Applied Surface Science*, *356*, 762–768. https://doi.org/10.1016/j.apsusc.2015.08.070